

# Bio-inspired photonic and plasmonic systems for gas sensing: applications, fabrication, and analytical methods

Amanda L. Musgrove<sup>a,\*</sup>, Alexander Cockerham<sup>b</sup>, Javier J. Pazos<sup>c</sup>,  
Shaimum Shahriar<sup>d</sup>, Michael McMahon<sup>b</sup>, Jimmy E. Touma<sup>a</sup>, and  
Stephen M. Kuebler<sup>b,d,e</sup>

<sup>a</sup>AFRL/Munitions, Optoelectronics and Photonics, Seekers Branch, Eglin Air Force Base, Florida, United States

<sup>b</sup>University of Central Florida, The College of Optics and Photonics, CREOL, Orlando, Florida, United States

<sup>c</sup>Heroica Technologies LLC, Brownsville, Texas, United States

<sup>d</sup>University of Central Florida, Department of Chemistry, Orlando, Florida, United States

<sup>e</sup>University of Central Florida, Department of Materials Science and Engineering, Orlando, Florida, United States

**ABSTRACT.** We review progress in the development of photonic platforms for detecting gases. Unlike sensors based on conventional refractive and diffractive optics, photonic sensors detect analytes using light–matter interactions of periodic nanostructures, plasmonic interactions, or combinations of the two. This summary focuses on the work done in the last two decades, and earlier reports are summarized in several authoritative reviews. Specifically, we focus on the research of bio-inspired photonic and plasmonic material fabrication, experimental studies, and theoretical studies for gas detection applications. In areas where reports are scarce, challenges are identified, and reports are included that may not directly relate to bio-inspired gas detection applications but nonetheless offer findings that can facilitate progress within underexplored areas of bioinspired gas sensing.

© The Authors. Published by SPIE under a Creative Commons Attribution 4.0 International License. Distribution or reproduction of this work in whole or in part requires full attribution of the original publication, including its DOI. [DOI: [10.1117/1.JOM.4.2.020902](https://doi.org/10.1117/1.JOM.4.2.020902)]

**Keywords:** biophotonics; gas sensors; nanofabrication; metaoptics; plasmonics; photonic crystals

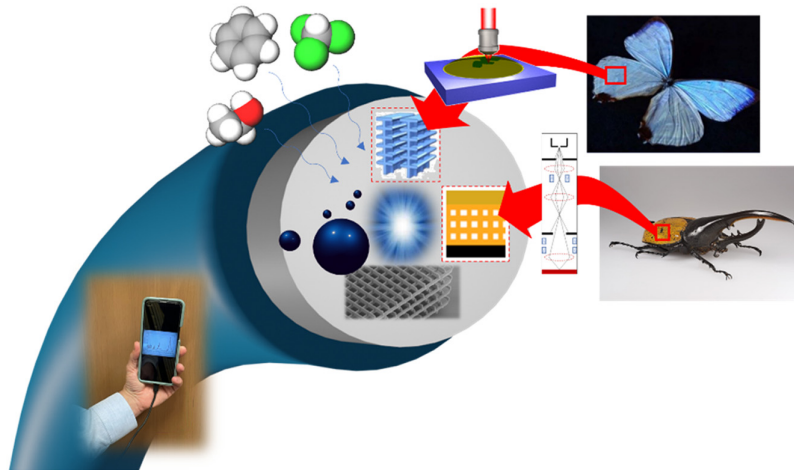
Paper 23029V received Sep. 12, 2023; revised Mar. 29, 2024; accepted May 1, 2024; published May 21, 2024.

## 1 Introduction

Intriguing photonic properties have been observed in a wide range of naturally occurring biological systems, and their corresponding functional structures and coatings can be synthetically fabricated and used to sense gases through optical response and measurement. Furthermore, adding metal nanoparticles to bio-inspired structures introduces plasmonic effects that can augment the light–matter interaction and improve sensing. This review discusses fabrication methods for engineering photonic crystals (PhCs), three-dimensional (3D) nanostructures, photonic coatings, and related devices for gas sensing. The concept is illustrated in Fig. 1. The review focuses on progress over the last two decades. Earlier accounts are summarized in several authoritative works.<sup>1–6</sup>

Our discussion is divided into the following focus areas. Specific to photonic materials, a review of experimental studies is provided to summarize recent reports of how morphology and structural changes of bio-inspired photonic structures impact the resulting optical response

\*Address all correspondence to Amanda L. Musgrove, [musgroveal@ornl.gov](mailto:musgroveal@ornl.gov)



**Fig. 1** Concept of the bio-inspired photonic/plasmonic gas sensor. Figures modified from Refs. 7 and 8 and reprinted with permission through Copyright Clearance Center and Creative Commons CC BY license.

measured, as well as how this impacts the gas detection capabilities of the material. This includes a discussion of photonic nanoparticles, holes and porous materials, and tree-like structures and pillars. The optical properties of many photonic structures found in nature can be understood within the framework of PhCs, dielectric stacks, and closely related diffractive devices. Examples of these are included throughout the work to motivate discussion of bio-photonic structures and to help readers identify new paths toward all-artificial bio-inspired devices that are optimized for specific applications. Furthermore, experimental work shows how defects and disorders can be controllably introduced into photonic materials to improve performance. Theoretical studies are also discussed for photonic materials and their applications. Specific to plasmonic materials, experimental findings on the properties of bio-inspired plasmonic coatings, as well as theoretical studies within the scope of this work, are also summarized. Methods for fabricating bio-inspired photonic and plasmonic materials are represented, followed by how the structure and defects in these materials impact their characterization and function in applications such as gas sensors.

### 1.1 Why Gases?

Chemical sensing provides a powerful means for detecting human, biological, and environmental activity. Sensing gases is particularly attractive because they are generated as primary or secondary analytes from so many processes, including those where the primary target to detect is another phase, such as liquid,<sup>9</sup> solid,<sup>10</sup> species in solution,<sup>11</sup> or a macroscopic particulate.<sup>12</sup> It is instructive to note a few examples of processes that generate gases because they provide insight into the diverse ways gas sensors can be applied.

As one example, depending on the nuclide involved, radioactive decay can produce isotopes of the noble gases helium,<sup>13</sup> radon,<sup>14</sup> xenon,<sup>15</sup> and krypton,<sup>16</sup> as well as halogens such as bromine<sup>17</sup> and iodine.<sup>18</sup> Detecting these products can be useful for geological surveying,<sup>19</sup> locating minerals,<sup>20</sup> stewarding nuclear waste,<sup>21</sup> ensuring nuclear security,<sup>22</sup> and detecting nuclear threats, such as “dirty bombs.”<sup>23</sup>

Explosives can also be detected directly if they are sufficiently volatile, or they can be detected indirectly through the outgassing of species entrapped during their production or as a result of slow decomposition.<sup>24–27</sup> Gas sensors for detecting di- and trinitrotoluene (TNT) are known,<sup>28–30</sup> but because higher-energy explosives such as 1,3,5-trinitro-1,3,5-triazine are so much less volatile, there is a pressing need for new, high-sensitivity detectors.<sup>31</sup>

Bacteria generate gases as part of their metabolism or decomposition, which can be detectable by sensors.<sup>32,33</sup> Bacterial contamination of fresh fruits and vegetables has become a major problem with significant health and economic impacts. Major illness and death have resulted from cross-contaminations in the food-production chain by *Clostridium botulinum*, *Escherichia coli* O157: H7, *Listeria monocytogenes*, *Salmonella*, *Shigella*, *Staphylococcus*, and *Vibrio cholera*.<sup>34</sup> Studies in cultured samples showed that *E. coli* produces a range of volatile

organic compounds (VOCs).<sup>35</sup> Parallel detection and quantification of VOCs could provide a signature for identifying bacterial contaminants. Anaerobic bacteria that break down organic matter generate methane (CH<sub>4</sub>)-comprising swamp gas.<sup>36</sup> Anaerobic bacteria that inhabit the mouth generate malodorous polyamines and volatile sulfur-containing compounds, such as hydrogen sulfide and methyl mercaptan that have a rotten egg smell. These compounds contribute to halitosis, but in high concentrations, they can indicate dental disease.<sup>37</sup>

From a historical perspective, it was known to the ancients that odor on breath can indicate disease.<sup>38</sup> A cloying sweet odor can indicate ketosis for diabetics. More recent work has shown that biomarkers associated with Parkinson's disease can be detected from breath,<sup>38</sup> and it has also been used to screen disease among children<sup>39</sup> and to monitor wound repair and healing.<sup>40</sup> Detecting VOCs such as isoprene and acetone on the breath can be used to assess the emotional response of individuals and groups, which can be useful for security screening, forensic science, and developing environments that lower stress.<sup>41</sup>

Monitoring volatile compounds has become increasingly important in agriculture. Ethylene, ethylene oxide, and nitric oxide are all involved in the ripening of some fruits.<sup>42</sup> Nitric oxide has been used to delay ripening,<sup>43</sup> whereas ethylene accelerates ripening.<sup>44</sup> Ethylene is also produced by fruits and vegetables, so ethylene concentrations must be controlled when they are stored to prevent premature ripening and food waste.<sup>45</sup> Gas monitoring has also been explored as a means for assessing crop health, particularly algal cultivation,<sup>46</sup> which may become important for sustainable biofuels and alternative foods.

Another gas generation source comes from the production of CH<sub>4</sub> from animals, which is a potent greenhouse gas. Kidney problems lead to an accumulation of urea, which decomposes to ammonia (NH<sub>3</sub>) that is detectable in urine and on an animal's breath.<sup>47</sup> In poultry farms with inadequate ventilation, NH<sub>3</sub> formed from the decomposition of waste can accumulate, harming the animals.<sup>48</sup> Furthermore, gas detection can be used to assess and ensure animal health, as well as to quantify carbon footprint.

High-sensitivity gas sensors are particularly sought for forensic science and law enforcement.<sup>49</sup> Accelerants leave trace VOCs that can enable investigators to identify the source and cause of fire. Remote sensors can be used for alcohol and drug detection and passenger screening. Detection of polyamines such as putrescine, cadaverine, and mercaptans produced by decomposition can be used to detect human remains. High-sensitivity remote optical sensors would also be useful for detecting combustible liquids, gun powder, and explosives.

Some find the “new-car” smell attractive, but chronic exposure to VOCs that outgas from adhesives, rubbers, and plastics can negatively impact health. Outgassing of noxious chemicals from substandard building materials has been linked to health problems and pipe corrosion.<sup>50</sup> Early-phase mold detection can also be useful for preventing health problems and minimizing damage that originates from water leaks or accumulating moisture.

The examples above show how gas sensing can be used in a myriad of applications that includes agriculture,<sup>51</sup> environmental stewardship,<sup>52</sup> health,<sup>53</sup> security,<sup>54</sup> defense,<sup>55</sup> forensics,<sup>56</sup> and psychology.<sup>57</sup> These needs are driving research to develop new gas sensors with higher specificity, lower limits of detection (LOD), and higher sensitivity. At the same time, each of these applications brings unique constraints that require new technologies for gas sensing—particularly optical sensing—to meet needs related to cost, reliability, agility, deployability, and proximity to measurement. These needs could be met by drawing inspiration from remarkable examples of biological adaption that generate exquisite optical performance in simple, compact forms that we are only just beginning to understand.

## 1.2 Opportunities and Challenges

Detecting a gaseous analyte presents both opportunities and challenges. Many natural and anthropogenic processes generate gases that can be identified as either primary or secondary products. Gases often accompany primary targets, which may be present as liquids, solids, or complex matrices. Detection involving a solid or liquid analyte usually requires that the instrument is brought to the source. That may not be possible if the analyte is obscured perhaps because it is sealed in a shipping container, buried underground, or embedded within a tissue or organ. By contrast, gases can diffuse and escape from the source. This can enable remote detection or detection within the vicinity. In these instances, gases are often diluted, particularly if they have

diffused, so gas sensing in these circumstances typically involves reading weaker signals and requires higher sensitivity than sensors directly detecting solids and liquids at their point of origin.

Optical methods can leverage many of the advantages of gas detection while surmounting some of the challenges.<sup>58–62</sup> Gases can be directly detected by their response at infrared (IR) wavelengths due to rotational and vibrational modes. In multi-atom species, the vibrational modes can be associated with functional groups comprising the molecule, and together, they form a “fingerprint” that can be used to identify specific gases or classes of analytes. With proper benchmarking, the magnitude of an IR signal can be correlated with the concentration of an individual species. Light propagating in free space can be used for stand-off detection.<sup>63,64</sup> Optical fibers and endoscopic tools can be used to bring light to a source with less loss, interference, and disruption, even along circuitous paths that would obstruct the free propagation of light.<sup>65,66</sup> While optical methods provide some advantages to electronic detection, several complexities in integrating optical methods can present challenges. For example, electronic sensors require power sources at the detection site and are subject to interference.<sup>67,68</sup> Optical sensors also introduce new possibilities for clandestine sensing (along with a myriad of potential ethical issues).<sup>69,70</sup> Additional challenges related to integrating optical methods into gas detection sensors are discussed below.

### 1.3 Optical Transduction

Most gases cannot be directly detected using visible radiation, but it is possible for some species such as nitrogen dioxide (NO<sub>2</sub>), which appears red-brown. Tremendous progress has been achieved in the sensing and detection of gases with instruments based on conventional refractive and diffractive spectrometers.<sup>71,72</sup> However, these instruments are not well suited for a growing range of applications that impose more stringent requirements. These include the need for small, compact, light-weight systems; improved LOD and limits of quantification; and improved specificity.<sup>73–75</sup> Capabilities for the application of systems with remote detection and high specificity are currently limited, and the development of materials with such capabilities is of high interest.<sup>76,77</sup> One approach that can be used to improve detector capabilities is the exploitation of optical responses from photonic and plasmonic materials that are integrated into the device.<sup>4,78,79</sup>

### 1.4 Optical Response

The presence of an analyte can introduce a measurable optical response from many factors, including change in absorption, variation of refractive index, phase modification and modulation, modification of interference patterns, and alteration of diffraction patterns.<sup>80–85</sup> Analytes that exhibit optical resonance at known frequencies can be observed by measuring optical absorption.<sup>86</sup> Given a known pathlength, the concentration of an analyte can be determined as well using established mathematical constructs such as the Beer–Lambert law.<sup>87,88</sup> Many chemical species can be identified and quantified by measuring one or more absorptions in the near IR regime, where optical absorption occurs due to characteristic molecular vibrations.<sup>89</sup>

Even when a gaseous analyte does not have an optical resonance at a frequency available for measurement, there can still be a change in the optical response of a system in the presence of a gas or vapor.<sup>90</sup> For example, an analyte may have a large real component of its dielectric function at a frequency of interest, which will result in the change of the optical pathlength in a system even when the geometry of the system is unchanged. A change in the refractive index can be observed using well-known techniques such as refractometry and interferometry.<sup>91,92</sup> One such technique is to measure the angle of refraction when light is incident on a region containing an analyte, enabling the determination of a refractive index using Snell’s law.<sup>93</sup> Interferometric techniques such as Mach–Zehnder-type interferometers can be used to detect an analyte at low concentration from its slight change in the medium’s refractive index, which produces detectable shifts in the interference fringes.<sup>94,95</sup>

The optical response also depends on whether a medium is dielectric or metallic. In dielectric media, light interacts with a material by polarizing locally bound valence electrons.<sup>96</sup> Light incident on a molecule induces an oscillating polarization parallel to the allowed transition moments of the system.<sup>93</sup> The system can be modeled as a harmonic oscillator, where the driving force is the oscillating electric field, and the response of the valence electrons to the field is the oscillator

itself.<sup>97</sup> Mathematically, this is often represented as a Lorentz oscillator.<sup>93</sup> When the frequency of the driving force is on-resonance with the dielectric material, light is absorbed. Near the resonance peaks of a material, the phase velocity of light is affected. When the frequency is off-resonance but just below a peak, the phase velocity of light is reduced. When the driving frequency is above resonance, the phase velocity is increased.<sup>98</sup> In isotropic media, the optical response is independent of the polarization of incident light. Whereas in anisotropic media, the optical response depends on the orientation of the material with respect to the polarization of incident light.<sup>99</sup>

Relative to dielectrics, metals respond to light quite differently because the valence electrons of adjacent atoms overlap strongly, forming highly delocalized bands that are often described as electron gas.<sup>100,101</sup> In terms of the harmonic oscillator model, this represents an oscillator without a resonance frequency.<sup>102</sup> This can be represented with the Drude model, which is equivalent to the Lorentz model with a resonance frequency of zero.<sup>102,103</sup> When valence electrons are displaced in a metal, the Coulomb force resulting from electron motion acts as the restoring force.<sup>104</sup> The frequency of the restoring force is represented by the plasma frequency of the material, which is a material property dependent on electron density.<sup>105</sup> For small spherical nanoparticles, this can be represented as surface charges, which build up on a particle as light couples to the oscillation of the valence electrons of the metal.<sup>106</sup> When surface charges build up on the particle, the fields near the surface of the particle are greatly enhanced in magnitude. This phenomenon is called surface plasmon resonance, and the frequency at which this resonance occurs can be changed depending on material properties, particle shape, and surrounding media.<sup>106,107</sup> The area of light–matter interaction concerned with surface plasmons is called plasmonics.<sup>108</sup>

Optical responses depend on the structure of the material on both the atomic and wavelength scales. Dielectrics can be structured to interact with light in a way that alters and even enhances the light–matter interaction.<sup>109–112</sup> For example, dielectric waveguides confine light to propagate in certain guided spatial modes.<sup>113–115</sup> The frequency of these guided modes depends on the structural orientation, as well as the material properties of the dielectric and the surrounding medium. More complex structures such as metasurfaces and PhCs enable interference and diffraction between light that can interact with nanoscale features.<sup>110,116,117</sup> The structural orientation provides identifiable optical responses that can be tuned, and the presence of an analyte can alter this optical response in a measurable way.

Likewise, for plasmonic devices, the optical response of a metal nanoparticle is greatly affected by the shape and size of the particle, as well as adjacent surfaces.<sup>106,118</sup> Field enhancement brought about by coupling to surface plasmon resonance is highly dependent on surface geometry. This phenomenon is the basis for many analytical techniques, including surface-enhanced Raman scattering (SERS), dark-field microscopy, and detection of analytes.<sup>119–123</sup> In the case of analyte detection, the frequency and strength of surface plasmon resonances can be greatly affected by the presence of analyte.<sup>124</sup> This is because the frequency of a localized surface plasmon resonance is dependent not only on the refractive index of a nanoparticle but also on the refractive index of the surrounding material. When a gas or vapor is present, the surrounding refractive index is changed and moves the frequency of the resonance peak.

Dielectric and plasmonic devices can be used in conjunction with gas-sensing applications as well.<sup>125,126</sup> For example, a dielectric prism coated with a metallic film can be used to couple incident light to surface plasmon polaritons.<sup>127</sup> These are surface waves that propagate along a metal–dielectric interface when light is totally internally reflected within the prism. Evanescent waves that have the same momentum as the surface plasmon polariton absorb all incident light when the damping from losses and radiation is equivalent.<sup>128,129</sup> This condition is called the critical coupling condition. At a given incidence angle, the frequency of the surface plasmon polariton is highly dependent on the refractive index of the surrounding medium, and thin layers of particles on the order of several nanometers can be readily detected by the shift in the peak of the surface plasmon polariton.<sup>130</sup>

## 2 Fabrication Methods of PhCs and 3D Nanostructures

The vivid structural coloration of some butterflies,<sup>6,131</sup> peacocks,<sup>132–135</sup> and other birds<sup>136,137</sup> has inspired an exciting new class of gas sensors.<sup>138,139</sup> The wings and feathers of these creatures are comprised of intricate nanostructures that often resemble rods, spheres, or a dense matrix of the two. When the matrix of nanostructures is periodic and ordered, its optical response can

be modeled as a PhC.<sup>135</sup> The optical response of a PhC is very sensitive to its composition and environment, which is a desirable quality for high-performance gas sensors.<sup>4,78</sup> Sometimes, natural nanostructures are topologically complex and even partly disordered, so they cannot be modeled as a basic PhC.<sup>140</sup> One example is the open-air tree-like structure of the *Morpho* butterfly,<sup>141,142</sup> which has been studied extensively both for its optical properties<sup>143,144</sup> and related sensing applications.<sup>8,145</sup> In these cases, multiple models are needed to simulate the performance of the complex 3D structure, particularly to account for variations in long-range order.<sup>146,147</sup>

Of course, using these biologically inspired structures as sensors necessitates their fabrication. The art of PhC fabrication has been addressed by many.<sup>148–153</sup> PhC fabrication can be separated into two main types: top-down and bottom-up. Top-down methods are used to create structures by patterning or etching,<sup>152</sup> whereas bottom-up methods employ molecular components and the natural forces between them as building blocks for larger structures.<sup>128,151,153</sup> Some popular top-down methods include particle- and electron-beam lithography,<sup>154–156</sup> holographic/interference lithography (IL),<sup>157–160</sup> and nanoimprint lithography,<sup>161,162</sup> to name a few. Self-assembly and thin film deposition are the key methods used in bottom-up approaches.<sup>163</sup> Table 1 summarizes and compares the key fabrication methods for fabricating photonic sensors. It is important to note that the goal of this section is not to teach how these methods work but to review how they are applied to fabricate these materials.

## 2.1 Particle Beam Lithography

Electron beam lithography (EBL) has long been recognized as a well-suited method for fabricating sub-micron planar patterns due to its inherently high resolution.<sup>168,169</sup> In EBL, a beam of accelerated electrons is serially scanned over an electron-sensitive polymer layer in a predefined pattern.<sup>170</sup> The incident electrons have sufficient energy to induce ionization of the polymer. In turn, secondary electrons are generated. These secondary electrons induce either crosslinking or degradation, which changes the solubility of the polymer, allowing certain portions to be rinsed away with solvent. With the remaining exposed polymer, thin film deposition methods or etching processes can be applied to create a final structure. Scanning electron microscopy (SEM) images of PhCs fabricated using EBL can be seen in Figs. 2(a) and 2(b).

A variety of PhCs have been fabricated by EBL, including two-dimensional (2D) and 3D PhCs.<sup>155,156,171</sup> EBL can also be used to introduce buried defects in PhCs, which is important when attempting to mimic nature's disorder.<sup>154</sup> Because structures in nature are usually not perfectly flat, there is a need for patterning on non-planar substrates, which EBL accommodates.<sup>172</sup> Traditionally, EBL was restricted to 2D patterns, but layering and stacking enabled the creation of 3D patterns. Layering is time-consuming due to repetitive exposures, and stacking introduces the potential for alignment inaccuracies.

Potyrailo et al.<sup>8</sup> used a clever, single-exposure approach to create butterfly-inspired 3D structures, as seen in Fig. 2(c). The structures included a 2D pattern projected onto the substrate interleaved with a periodic structure in a direction along the exposure beam and perpendicular to the substrate. The sample was prepared by first depositing alternating thin layers of poly(methyl methacrylate) and poly(methacrylic acid). The layer thickness was chosen to match the targeted periodicity perpendicular to the substrate. The sample was then exposed using carefully controlled, spatially varied electron beam dose. A high dose was used in regions where the material of both layers needed to clear all the way to the substrate, mimicking the 2D projected pattern. A low dose was used in regions where periodicity along the exposure beam was desired. In these low-dose regions, only the material comprising the high-sensitivity layers was activated. During the development step, the exposed high-sensitivity material was etched away, which left open voids between overhanging regions of the high-sensitivity material.

The approach and instrumentation used for focused ion beam (FIB) lithography are similar to that involved with EBL, with a key exception being that accelerated ions interact with the sample rather than electrons.<sup>173,174</sup> FIB has more capabilities due to the wide selection of ion sources. For example, a helium ion source enables traditional lithography through exposure, development, and post-processing of a polymer layer. In what some call FIB chemical vapor deposition (FIB-CVD),<sup>175,176</sup> gallium and neon ions can be used to induce deposition from gaseous components onto a substrate. This enables mask-free, 3D writing of nanostructures through deposition rather than through the removal of the material.

**Table 1** Comparison of methods for fabricating photonic sensors.

Method	Resolution	Max area	Material type	Comments
Photolithography <sup>102</sup>	5 nm, 1 $\mu$ m typical <sup>a</sup>	100 cm <sup>2</sup>	Photopolymers	2D and 3D <sup>b,c</sup>
E-beam lithography <sup>87-89</sup>	5 nm	1 cm <sup>2</sup>	Resists, pattern-transfer by etching	Mostly 2D <sup>b,d</sup>
Ion-beam lithography <sup>101,102</sup>	10 nm	1 cm <sup>2</sup>	Metals, oxides, semiconductors	2D <sup>b</sup>
Holographic lithography <sup>90-93</sup>	>200 nm	1 cm <sup>2</sup>	Photopolymers	2D and 3D
Nanoimprint lithography <sup>94,95</sup>	5 nm	10 cm <sup>2</sup>	Silicones	2D and 2.5D <sup>e</sup>
PVD <sup>64</sup>	10 nm	Limited by chamber	Metal, oxides, semiconductors, organics	Coating existing structures
CVD <sup>65,166</sup>	10 nm	Limited by chamber	Metal, oxides, semiconductors, organics	Coating existing structures
ALD <sup>67</sup>	10 nm	Limited by chamber	Metal oxides, semiconductor	Coating existing structures
Etching <sup>85</sup>	10 nm	>100 cm <sup>2</sup>	Multiple types	Pattern transfer and reshaping <sup>f</sup>
Self-assembly <sup>96</sup>	Can be <50 nm	1 cm <sup>2</sup>	Colloids	Limited control of structure

<sup>a</sup>Small-area 3D structures can be created by multiphoton lithography (see S. M. Kuebler and M. Rumi. "Nonlinear optics—applications: three-dimensional microfabrication," in Encyclopedia of Modern Optics, R. D. Guenther, D. G. Steel and L. Bayvel, Eds. Elsevier: Oxford, 2004, pp. 189–206).

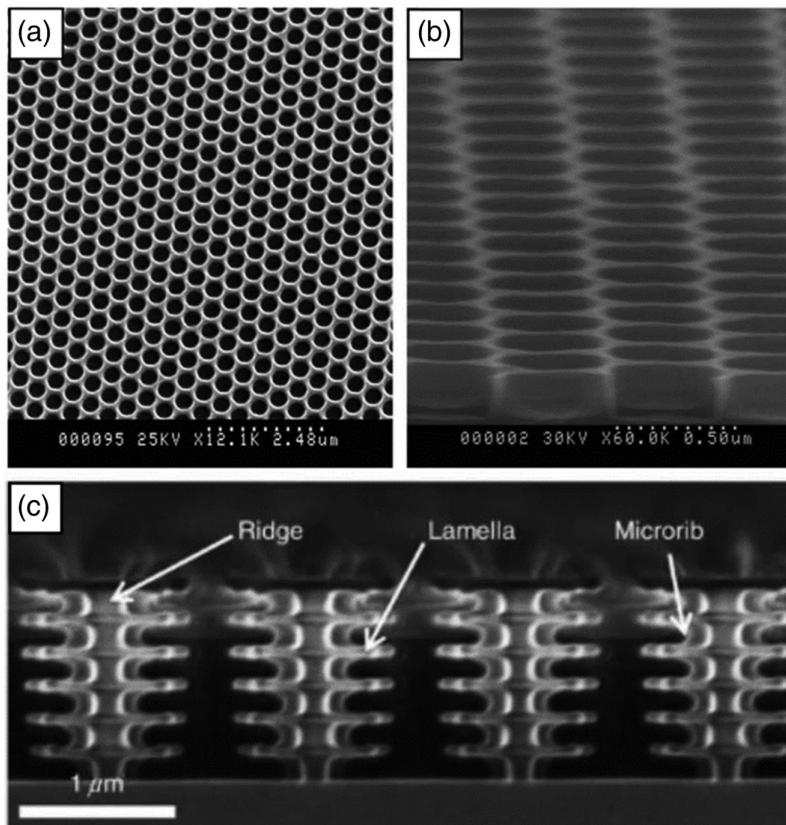
<sup>b</sup>High-symmetry 3D structure achieved using multi-layer resist patterning.<sup>78</sup>

<sup>c</sup>Resolution depends on the patterning wavelength and complexity of the optical projection system. Cost increases dramatically as feature size decreases.

<sup>d</sup>3D possible by complex multi-layer exposure.

<sup>e</sup>Useful for replicating 2D patterns and 3D structures with limited undercut and no enclosed voids.

<sup>f</sup>Etch-area is practically limited by the complexity of structure and how that affects chemical diffusion.



**Fig. 2** SEM images of PhCs fabricated by EBL. (a) Top-down view of 2D PhC. (b) Perspective view of the same PhC. Figures adapted from Ref. 155 and reprinted with permission through Copyright Clearance Center. (c) Fabricated structures using EBL, inspired by the *Morpho* butterfly wing topology. Figure modified from Ref. 8 and reprinted under the terms of the Creative Commons CC BY license.

## 2.2 Photolithography

Photolithography<sup>177</sup> is used extensively in the semiconductor industry due to its high throughput and comparably low lifetime cost.<sup>178</sup> Whereas EBL is a serial, point-by-point writing process, some forms of photolithography flash the entire writing area with a single exposure.<sup>179,180</sup> In conventional photolithography, pattern generation is accomplished with area-selective projections using either one or multiple masks. The incident photon energies induce crosslinking or chain-scission in the photopolymer. This enables the use of solvents to wash away exposed or unexposed areas. Thin film deposition and etching techniques can be utilized to transfer the pattern in the developed photopolymer to other materials, such as dielectrics or metals.

Using conventional photolithography and etching techniques, tree-like structures have been fabricated. Using these techniques, Rasson et al.<sup>181</sup> created a bio-inspired vapor sensor inspired by the *Papilio* butterfly wing. Their device featured concave, sloped walls achieved by a mix of isotropic and anisotropic electrochemical etching of silicon. Potyrailo et al.<sup>182</sup> used conventional photolithography with plasma-enhanced chemical vapor deposition (CVD) and etching to create bio-inspired sensors for non-condensable gases. Motivated by the structural color of the *Morpho* butterfly, the group fabricated sensors that successfully detected H<sub>2</sub>, CO, and CO<sub>2</sub>. To detect different gases, the team enhanced the structure with additional elements. For example, to detect CO and H<sub>2</sub>, the structure was covered in a layer of gold nanoparticles (AuNPs) 3 to 5 nm in diameter. Furthermore, to detect CO<sub>2</sub>, the structure was covered with amorphous Teflon.<sup>182</sup>

## 2.3 Interference/Holographic Lithography

IL, also known as holographic lithography,<sup>157</sup> uses multiple beams to create periodic interference patterns in a 2D or 3D manner.<sup>183</sup> A reflective layer can be included or left out. By interfering



with four non-coplanar beams, with an appropriate choice angle of incidence and polarization, each of the 14 Bravais lattices can be created, which makes IL well suited for fabricating PhCs.<sup>184</sup>

A notable use of reflection-based IL was demonstrated by Siddique et al.<sup>185</sup> At a wavelength of 266 nm, “Christmas tree” structures resembling those seen on the *Morpho* butterfly wing were fabricated with lamella that were 40 nm thick with air gaps between the layers of lamellae. This resulted in the expected blue reflected light. The key to the successful fabrication was a highly reflective surface on the substrate, which is normally undesirable for traditional IL, as the reflected light further interferes with the expected pattern. The reflective surface strengthened the intensity of the vertical standing waves, which ultimately created the lamella.

### 3 Fabrication of Surface Coatings for Enhanced Sensing

Some optical effects can be improved by depositing thin metal films or nanoparticles onto active surfaces to redirect or augment local electromagnetic fields via surface and localized surface plasmons.<sup>3,186,187</sup> The approach has been used in several optical applications, including solar cells, spectroscopy, signal enhancement for imaging, sensors, and cancer treatment.<sup>188,189</sup> This section focuses on metal- and nanoparticle-coated bio-inspired photonic structures.

#### 3.1 Thin-Film Deposition Methods

Thin films can be deposited onto surfaces through physical vapor deposition (PVD) or CVD. In PVD, a target containing the material to be deposited is vaporized by some form of energy within a vacuum chamber. The surface being coated is placed inside the chamber and is subjected to the vapor. Because PVD is a directional deposition method, the substrate is usually mounted and rotated to achieve full-angle coverage. The different types of PVD are differentiated by their energy source. Specifically, thermal PVD uses a resistively heated filament, sputter PVD uses energetic particles from plasma, and ion beam-assisted deposition uses a beam of ions to accelerate vaporized species toward the surface of the substrate.<sup>164</sup>

Seeking to enhance the response of a *Morpho* butterfly-inspired light sensor, Zhang et al. used PVD to deposit 50 nm thick layers of gold onto the Christmas-tree structure.<sup>190</sup> Due to PVD’s directional nature, only the tips of the lamella layers were covered. This resulted in increased local absorption of IR radiation, which curled the lamella upward, decreasing IR reflectance and successfully detecting the presence of IR light.

In CVD, the materials to be deposited are volatile and in a different form than the final deposit. Precursor gases are released into a chamber, which then become adsorbed onto the surface of the substrate. Due to the isotropic diffusion of gases within the chamber, usually under high pressure, CVD is naturally conformal. The different types of CVD are differentiated by their chemical composition or pressure such as low-pressure CVD<sup>165</sup> or metal-organic CVD.<sup>166</sup>

Atomic layer deposition (ALD) is a common form of CVD in nanofabrication where two precursors are delivered into a chamber, one at a time. Once the first precursor is delivered, the chamber is purged with inert gas, removing all but the adsorbed precursor. Then, the second precursor is delivered. Due to the adsorption of the first precursor on the substrate, the second precursor forms a complete monolayer upon successful reaction. This process repeats to form a conformal thin film with excellent thickness control.<sup>167</sup>

Piszter et al. used ALD to coat a *Polyommatus icarus* wing in 5 nm of Al<sub>2</sub>O<sub>3</sub>.<sup>191</sup> While the change in performance was not desirable for sensor applications, the researchers showed that the desired sensor performance is dependent on more than two predicted variables. In particular, the responsivity of the coated wing decreased by more than five times. The researchers determined that capillary condensation was the primary driving force behind the observed color change of the butterfly wing.<sup>27</sup>

### 4 Characterization and Function of Photonic Materials

Photonic materials have recently gained interest in sensing applications because they can be used to manipulate and control the propagation of visible light. In gas sensing, exposure to specific analytes or volatile species can change the refractive index of materials, which shifts features in the ultraviolet-visible (UV-vis) spectrum. Understanding how morphological changes in PhCs

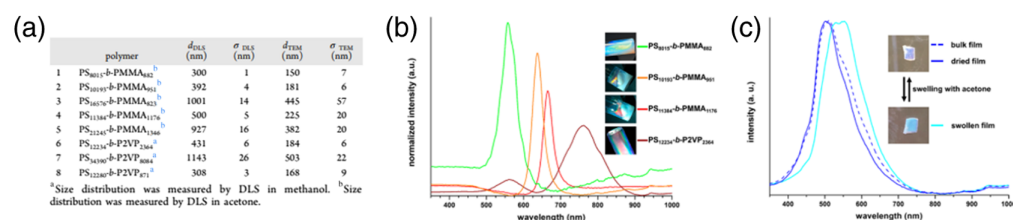
impact optical properties and interaction with analytes may aid in fabricating gas sensors with lower LOD and a wider range of analyte specificity. The following sections are grouped to discuss the function of photonic materials by morphology: photonic materials that are characterized as nanoparticles, fibers, porous materials, and tree-like structures. The impact of defects on function is also reviewed. We note that all the experimental studies of plasmonic and photonic materials discussed below were concerned with performance in the visible wavelength range (320 to 800 nm); however, some reported performance studies in the near-IR region (800 to 1700 nm) where the absorption line of CH<sub>4</sub>, hydrogen fluoride (HF), and NH<sub>3</sub> is present.<sup>192</sup>

#### 4.1 Nanoparticles

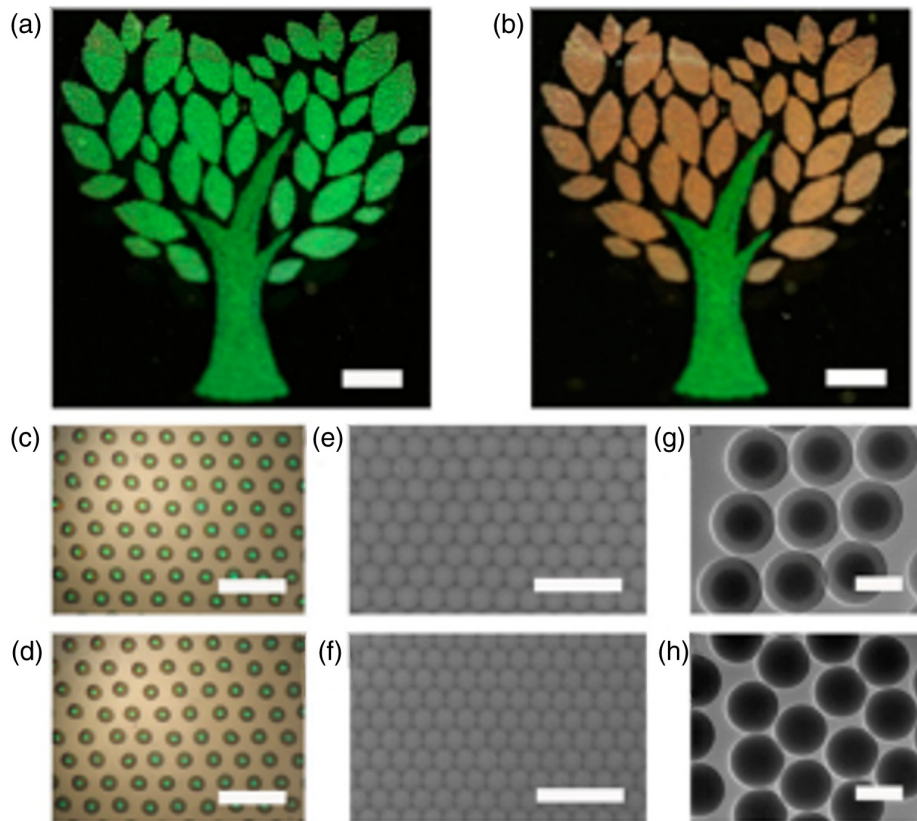
Spherical particles have been utilized to fabricate photonic materials for sensing applications, for which the size of the particle plays a direct role in the optical properties observed. Spherical colloidal particles have been shown to exhibit angle-dependent structural colors caused by Bragg diffraction with optical properties affected by the size of the particles synthesized. Appold and Gallei<sup>193</sup> synthesized block copolymers with varying molecular weights in the form of isotropic spherical micelles, which underwent colloidal crystallization. These materials were inspired by the structures observed in butterfly wings and beetle carapaces. To mimic the structural colors and artificial fabrication of photonic materials comparable to those inspired by biological photonic materials, Appold and Gallei stated that periodic domains of 120 nm or greater are required for the interaction and reflection of visible light. Dispersed in solution with diameters ranging from 300 to 1143 nm, the spherical colloidal particles fabricated resulted in reflectance spectra shifts from green to red, as seen in Figs. 3(a) and 3(b).

In addition, the block copolymers were fabricated into bulk films and exposed to acetone, which resulted in a reflectance shift due to swelling and an increase in the diameter of pores and a decrease in the refractive index contrast, as seen in Fig. 3(c). The size and disorder of the bulk films are shown to influence the structural colors stemming from diffuse particle scattering of the nanodomains as well. It is important to note that upon drying the film after exposure and swelling, the spectrum is comparable to the original, which suggests reversibility of the stimuli-responsive behavior.<sup>193</sup>

Also inspired by the multilayered scales on longhorn beetles, Bai et al.<sup>194</sup> fabricated mesoporous silica nanoparticles (MSNs) with adjusted particle sizes and proportion of pores to nanoparticles in the overall mesoporous material. These materials are tunable similar to the scales on the longhorn beetle such that changes in the thickness and average refractive index of their scales result in color shifts caused by water adsorption in their elytra. Mesoporous colloidal PhCs (MCPC), made of solid silica nanoparticles (SSNs), were inkjet-printed onto a substrate with a designed pattern and were assembled into well-ordered mesoporous “domes.” The composition of the particles played a vital role in the color changes observed. By adjusting the ordered arrangement of nanoparticles and using either solid core particles or mesoporous shells, vapor condensation in the pores from exposure to N<sub>2</sub> and ethanol vapors resulted in variations in the



**Fig. 3** (a) Dimensional analysis, including average diameter and standard deviation (nm), measured using microscopy imaging for BCP micelles. (b) Micellar PhCs were dispersed in methanol/acetone solution and measured at an angle of view of 90 deg, and UV-vis spectra of spherical colloidal particles comprised of polymers with varying sizes were collected. A green to red reflectance spectra shift was seen as the size of the particles increased. (c) Block copolymers were fabricated into films and exposed to acetone. UV-vis spectra collection revealed a reflective shift due to swelling and increased pore diameter, with a comparison of the bulk film (dashed blue line), swollen with acetone (cyan blue line), and the dried bulk film (blue line) measured at an angle view of 45 deg. Figure adapted from Ref. 193. Copyright 2019 American Chemical Society.



**Fig. 4** (a) and (b) Color changes observed of the printed pattern when in  $N_2$  versus saturated ethanol atmosphere (scale bar: 0.5 cm). (c) and (d) Optical microscopy images of the printed MCPC and  $SiO_2$  colloidal PhC (SCPC) microdots (scale bar:  $200 \mu m$ ). (e) and (f) Top-view SEM images of MCPC microdots and SCPC microdots (scale bar:  $1 \mu m$ ). (g) and (h) TEM images of MSNs and SSNs (scale bar:  $200 nm$ ). Figure reprinted with permission from Ref. 194. Copyright 2014 American Chemical Society.

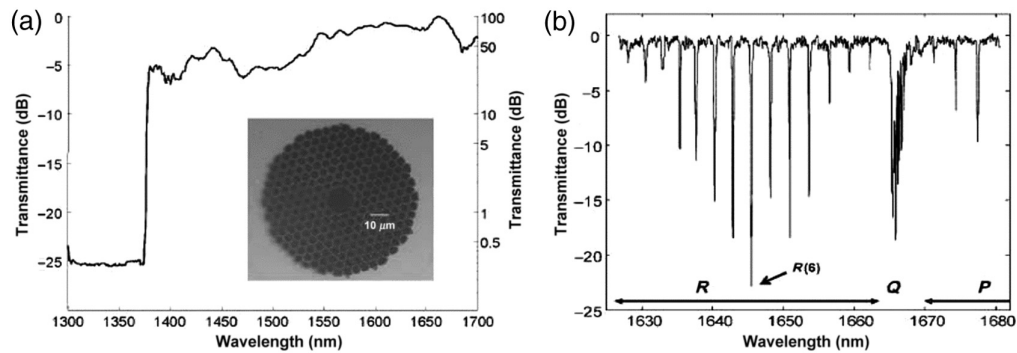
refraction index, which resulted in color changes, as seen in Fig. 4. The vapor-chromic features of the MCPC patterns were also reversible and repeatable, and the detection of vapors using these materials and fabrication method is easily visible by the naked eye, making this a practical and facile option for analyte detection in gas sensors.<sup>194</sup>

## 4.2 Fibers

Fiber-based optical systems have been investigated for use in gas-sensing applications, particularly through the implementation of PhC fibers.<sup>192,195–200</sup> One example is the use of hollow-core PhC fibers (HC-PCFs) due to their ability to permit guided light through media such as air or gases rather than through a dielectric core.<sup>197,201</sup> When an attenuating gas is used to fill the hollow-core of the HC-PCF, the transmission of light through the fiber can be recorded as a function of the concentration of analyte gas.<sup>202,203</sup>

The use of HC-PCFs for gas sensing has been examined by several groups,<sup>201,202,204</sup> including Cubillas et al.<sup>197</sup> who showed that  $CH_4$  was capable of being detected at concentrations as low as 10 ppmv. In this study and as seen in Fig. 5,  $CH_4$  filled the HC-PCF and was absorbed in the 1670 nm band; this resulted in a measurable absorbance in accordance with the Beer-Lambert law. Though  $CH_4$  does not have exceptionally high attenuation at 1670 nm, very long HC-PCFs were used to get a strong signal with a low signal-to-noise ratio.

Hu et al.<sup>201</sup> also worked on the use of HC-PCFs to detect gases, specifically acetylene. Typically, the limitations in HC-PCFs for gas detection include the length of time required to fill the fiber as well as coupling efficiency. To increase the rate at which the HC-PCF was filled with gas, two vacuum chambers were used in conjunction with a gas mixing chamber.

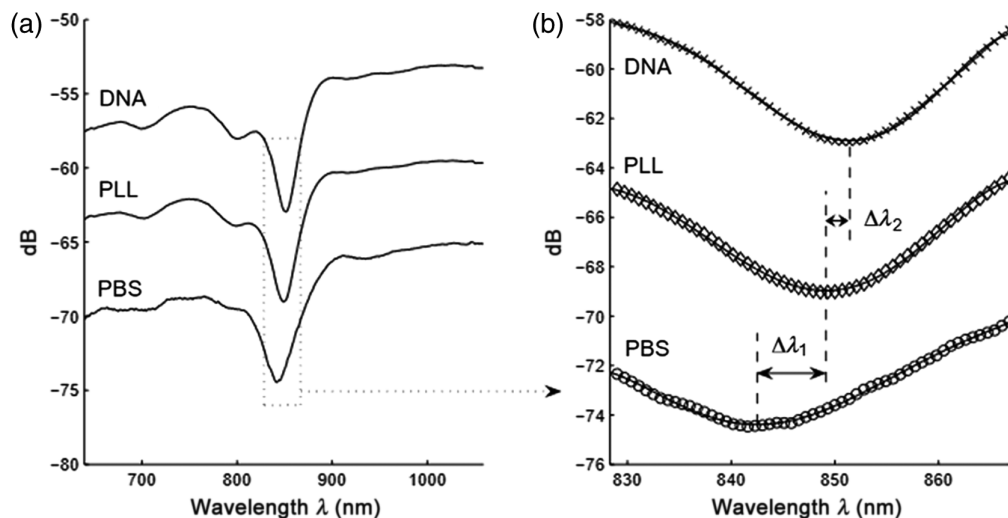


**Fig. 5** (a) Normalized transmission spectrum of HC-PCF; inset shows the image of the sample. (b) Transmission spectrum of HC-PCF filled with  $\text{CH}_4$  (18,750 ppmv). Adapted with permission from Ref. 197 © The Optical Society.

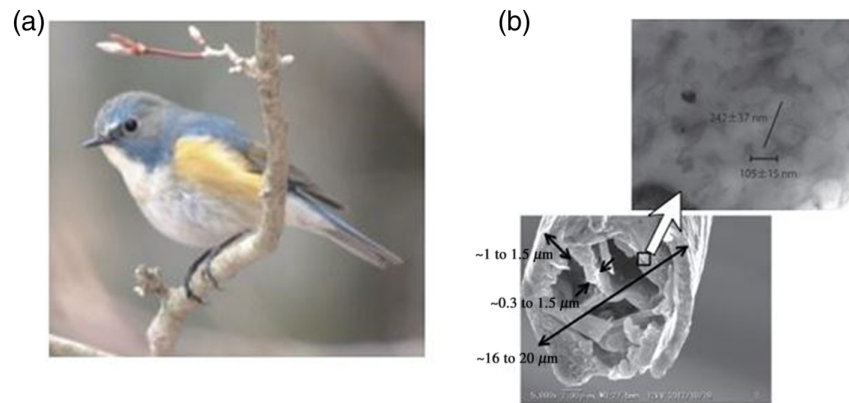
In addition, this system was created using precise fiber alignment devices to improve coupling efficiency. These modifications of the gas sensor system enabled the detection of acetylene at quantities as low as 0.084 ppm.

In addition to measuring the transmitted intensity of light through an HC-PCF to determine gas concentration, work has been done to investigate the use of long-period grating (LPG)<sup>205,206</sup> motifs in PCFs to monitor resonant wavelengths in the fiber to detect gas.<sup>10–12</sup> It was determined that periodic perturbations in PCFs allow for light to couple between the core and cladding modes of the fiber. The pitch of perturbations in the fiber determined the wavelength, which couples to these fiber modes. The variation in the refractive index within the fiber shifted the resonant wavelength of light. Furthermore, the introduction of gas to the hollow core of LPG-PCFs modified the refractive index, which caused changes in the resonant wavelength of the fiber.<sup>207</sup>

PCFs are not limited only to the detection of gas particles; PCFs have been used to detect biochemical markers as well.<sup>208,209</sup> Rindorf et al.<sup>210</sup> tested the sensing capabilities of LPG-PCFs toward various biomolecules. This method of biomolecule detection did not rely on the labeling of analyte species, providing a robust means of detection in a compact form factor. The change in resonant wavelength was used to determine film thickness for double-stranded deoxyribonucleic acid (dsDNA), poly-l-lysine (PLL), and phosphate buffer solution (PBS). Transmission spectra for each analyte are shown in Fig. 6.



**Fig. 6** (a) Overlay of transmission spectra in the near-IR region for LPG-PCFs containing films of either dsDNA, PLL, or PBS analyte. (b) Zoomed-in view of the minima for each analyte. Adapted with permission from Ref. 210 © The Optical Society.



**Fig. 7** (a) Image of the red-flanked blue-tail *T. cyanurus*. (b) SEM and TEM images showing the cross-section of barb fibers found on *T. cyanurus*. Figures adapted with permission from Ref. 136.

### 4.3 Holey and Porous Materials

Modifications in photonic materials containing holes and pores have also been shown to impact the resulting optical properties, thus modifying the potential detection limit of vapors. Holes have also been incorporated in controllable ways for applications in optical device integration. By inducing holes in this manner, photonic optical characteristics can be observed. Porous PhCs with interesting optical properties have been observed in nature, specifically by the red-flanked blue-tail, *Tarsiger cyanurus*, studied by Ueta et al.<sup>136</sup> The porous nature of the red-flanked blue-tail's barb fibers can be seen in Fig. 7. Ueta et al.<sup>136</sup> modeled and studied porous PhCs, which were bioinspired by these sponge-like, porous barbs in efforts to understand the optical properties correlated to the structural colors observed.

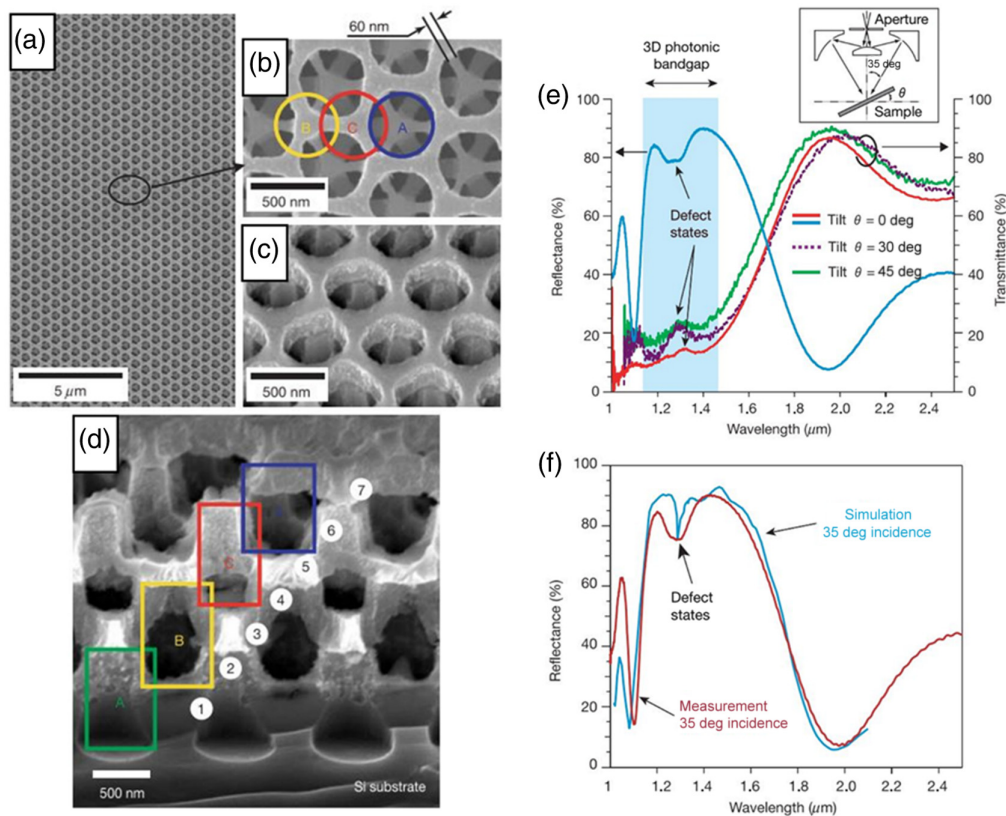
Porous photonic structures have also been seen in the scales covering the elytra of male *Hoplia coerulea* beetles, and interestingly, water-induced changes have been studied in which the fluorescence emission peak wavelength blue-shifts when the elytra are water immersed while the reflectance peak wavelength exhibits a red-shift.<sup>211</sup> These findings support the idea that optical properties can be studied based on the presence of adsorbed species.

Experimentally, porous materials have been successfully fabricated to study similar changes in optical properties. Qi et al.<sup>212</sup> were able to successfully fabricate PhCs with microcavities in a controlled fashion using lithography such that the array of holes and layers of microcavities were ordered, as depicted in Figs. 8(a)–8(d). Reflectance and transmittance data in the near-IR region were collected, and at varying incident angles, the reflectance and transmittance spectra are affected, as seen in Figs. 8(e) and 8(f), but more notably, the resonant signatures are around telecommunication wavelengths.<sup>212</sup>

PhCs with defects in the form of subwavelength holes to increase the surface area of the defect region have also been investigated. Multi-hole regions, defects in PhCs where several holes are present and are smaller than the lattice holes in the crystal, were studied by Kang et al.<sup>213</sup> due to the significant increase in surface area. In the case where a multi-hole defect (MHD) region was studied and compared with a single hole defect PhC structure, Kang et al.<sup>213</sup> concluded that the MHD region permitted a three times larger change in resonance frequency and two times larger quality factor.

Mesoporous film fabrication is another method that has been previously used in the development of sensors and creates an abundance of holes through the material. Kelly et al.<sup>214</sup> studied photonic nanostructures that were stacked together to form multiple mesoporous layers. These mesoporous structures have resulted in the adsorption of vapors, which can be tuned depending on the concentration gradient between the layers. In addition, the size and concentration of pores present in the layers can result in different rates of diffusion of analyte into the film, causing changes in the adsorption limit. Belén et al.<sup>215</sup> also showed enhanced optical properties using porous thin film anatase TiO<sub>2</sub> in which adding the additional nano-holed layer to titanium alloy provided both higher stability against thermal oxidation and enhanced near-IR reflectivity.

Nanogaps have also been implemented into a gold palladium (AuPd) surface in the form of cracks, as opposed to pores within the film, which had been layered into a polyimide/steel

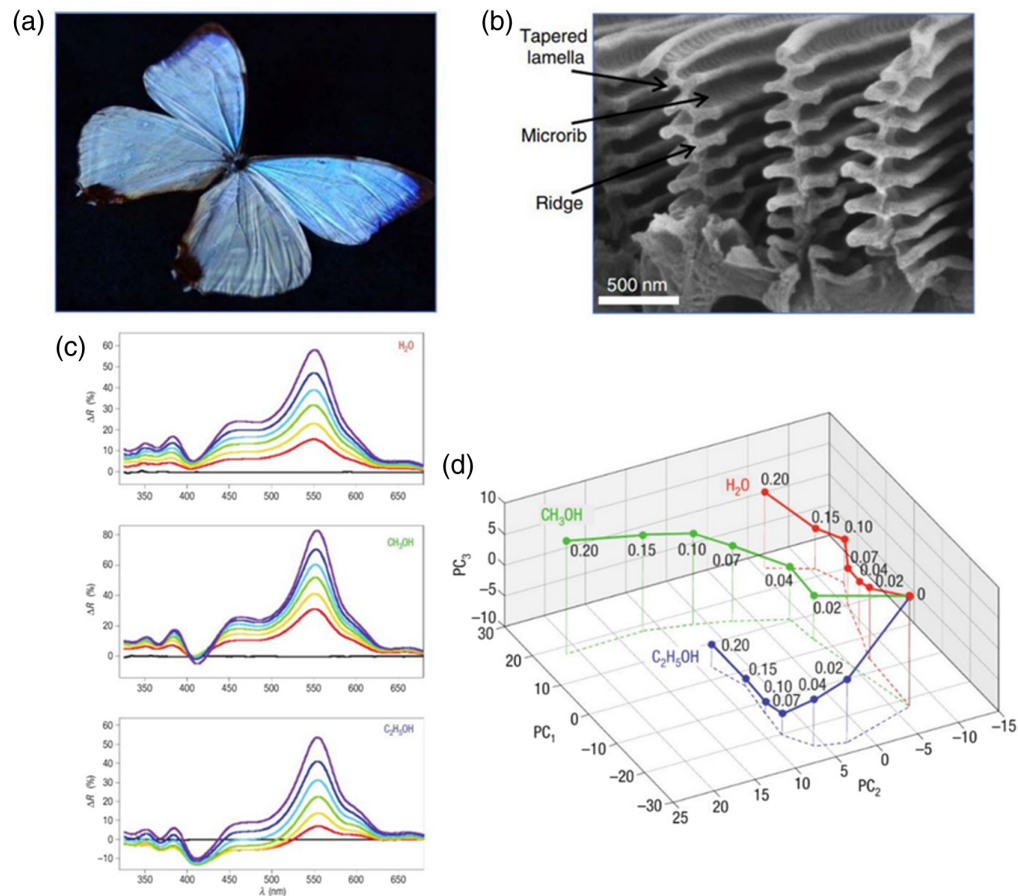


**Fig. 8** Scanning-electron micrographs of the fabricated 3D PhCs. (a) A low-magnification SEM top view of fabricated PhCs. (b) Close-up showing the hexagonal array of holes (denoted by A, B, and C) are the sets of holes underneath the top layer. A sequential shift can be seen in the horizontal direction. (c) A tilted top view reveals the rod layer underneath the holes. (d) A cross-sectional view, where the functional layers are marked by numbers and the etched air cylinders are outlined with rectangles. (e) FTIR-microscopy characterization of the 3D PhC with point defects, where reflection (blue) and transmission (red, purple, and green) are shown with varying sample tilts. An inset is included showing a schematic diagram of the optical path of the FTIR microscope. (f) A comparison of measurement (red) and simulation (blue) for reflection. Figures adapted from Ref. 212. and reprinted with permission through Copyright Clearance Center.

backing support by bending the fabricated sensor. When these nanogaps were present in the sensor,  $H_2$  detection was possible at concentrations as low as 100 ppm.<sup>216</sup>

#### 4.4 Tree Structures and Pillars

The *Morpho sulkowskyi* butterfly has scales on its wings that, under high magnification [Figs. 9(a) and 9(b)], are seen to have a tree-like structure in which lamellae and microribs give rise to interesting photonic optical properties.<sup>8</sup> These properties enable high-selectivity vapor sensing due to localized interactions with specific vapors and the chemical gradient of surface polarity these tree-like structures contain.<sup>217,218</sup> This has been shown in *M. sulkowskyi* wing scales by Potyrailo et al.<sup>218</sup> after realizing that the wings had a highly reproducible spectral reflectance peak due to the uniformity of the periodic nanoscale structure. These interesting optical properties are largely caused by the lamellae of the ridges acting as interferometric nanoreflectors, whereas the ridges act as diffraction grating.<sup>219</sup> These structures cause a multilayer interference from the array of reflectors, which gives rise to interesting properties due to diffraction and interference effects, as previously mentioned in a number of studies.<sup>8,164,186,187</sup> Potyrailo et al.<sup>218</sup> exposed *M. sulkowskyi* scales to multiple vapors at different concentrations and monitored the change in reflectance spectra ( $\Delta R$ ), finding differences in response when exposed to water, ethanol, and methanol. Specifically, significant changes in  $\Delta R$  were observed between 325 and 500 nm and in magnitude between 500 and 600 nm, as seen in Figs. 9(c) and 9(d).<sup>218</sup>



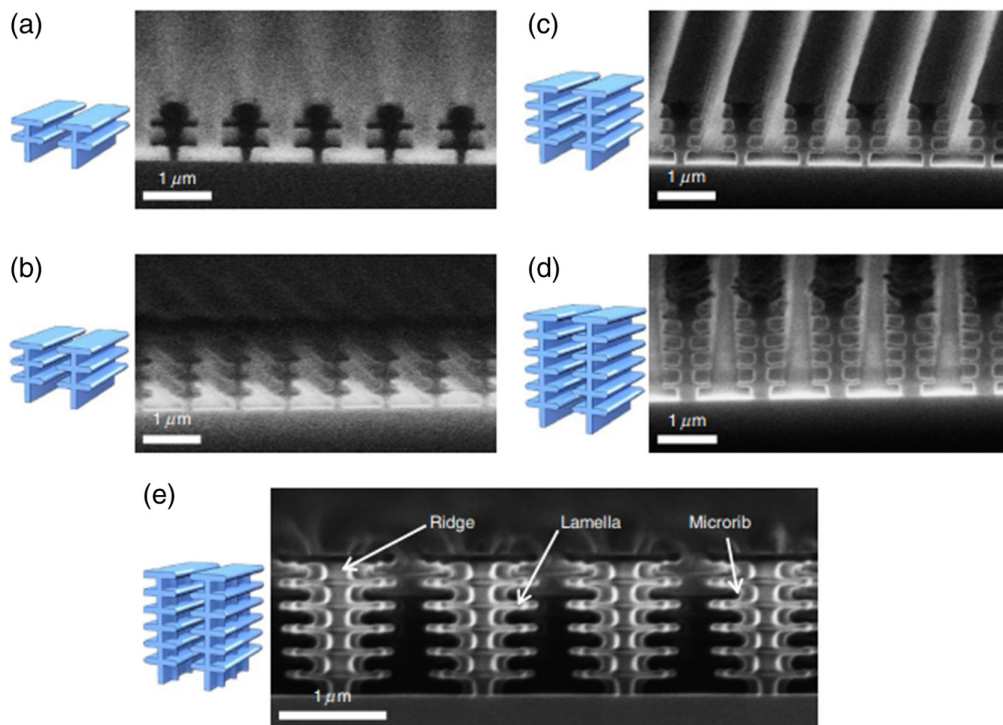
**Fig. 9** (a) An image of *M. sulkowskyi* scales, where iridescent coloration is notable. (b) SEM images of *M. sulkowskyi* scales found on the surface of the wings. Figure modified from Ref. 8 and reprinted under the terms of the Creative Commons CC BY license. (c) Analysis of the selectivity in the spectral response of photonic structure of *M. sulkowskyi* scales to different vapors, specifically water, ethanol, and methanol. (d) Discrimination of water, methanol, and ethanol vapors using PCA of  $\Delta R$ -spectra after mean-centering the spectra, showing both selectivity and sensitivity of the scales. Figure adapted from Ref. 218 and reprinted with permission through Copyright Clearance Center.

This prompted further studies to investigate how morphological changes in these photonic structures could further impact the optical responses recorded.

Using lithography, Potyrailo et al.<sup>8</sup> were able to fabricate nanostructures with varying dimensions and numbers of lamellae, in conjunction with performing computational analysis, in efforts to study the spectral changes in reflectance. Their fabricated nanostructures are seen in Fig. 10. Vapor-response stability and reproducibility were tested in addition to the differential reflectance  $\Delta R$  modes. Sensor stability and measurement precision were in good standing after 160 cycles, and spectral differences were observed dependent on the vapor in which the nanostructures were exposed, as seen in Fig. 11.<sup>8</sup> In addition to studying the effects on reflectance in the presence of different vapors, individual nodes and confined regions of the lamellae could be used to tune vapor sensing and distribute monitoring. This work showed that these nanostructures can be used as colorimetric sensors and tuned for a wide range of applications.<sup>8</sup>

## 5 Inducing Defects in Photonic Materials

Breaks from a perfect infinite lattice can be categorized as *defects* or as *disorder*. A defect is a targeted variation within a PhC, such as a point- or line-deletion, whereas disorder is the random variation of the parameters of a PhC—such as feature size, pitch, or refractive index—across the spatial domain of the lattice. The presence of defects may be used for sensing by creating localized resonances within the PhC that couple to molecular vibrations in the targeted analyte.<sup>165,166</sup>



**Fig. 10** (a)–(d) Schematics of nanostructures (left) and SEMs of nanostructures (right) with 2, 3, 4, and 6 lamellae, respectively. (e) A schematic (left) and SEM image of a nanostructure (right) with six lamellae and microribs. Figure modified from Ref. 8 and reprinted under the terms of the Creative Commons CC BY license.

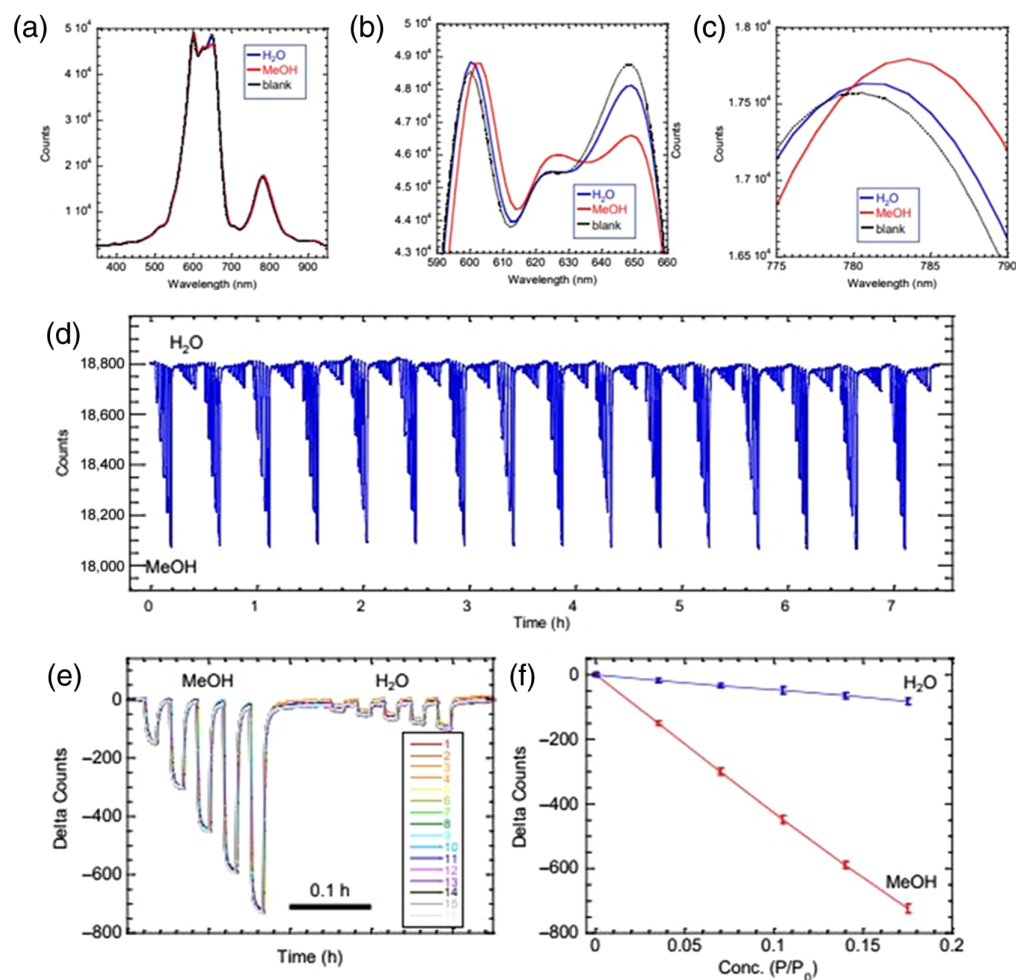
### 5.1 Defects

Although defects may be unintentionally introduced into a PhC device, deviation from a perfectly periodic PhC by purposefully including defects may be used to introduce sensing capabilities.<sup>165,167,220,213,221,222</sup> Extended random defects may be intentionally introduced to alter the range of the bandgap.<sup>165,223</sup> Numerous studies evaluating the introduction of extended defects have been performed.<sup>188,189,223–226</sup> The presence of an analyte can be modeled as a perturbation in a PhC device, and characterization of perturbed PhCs can be used to evaluate the performance of a PhC device in the presence of gas or biomolecules.<sup>166,196,227</sup> While not all works discussed below are bio-inspired, they may be relevant to those who are investigating bio-inspired systems with naturally occurring defects and disorder and are included to facilitate understanding of how defects impact characterization.

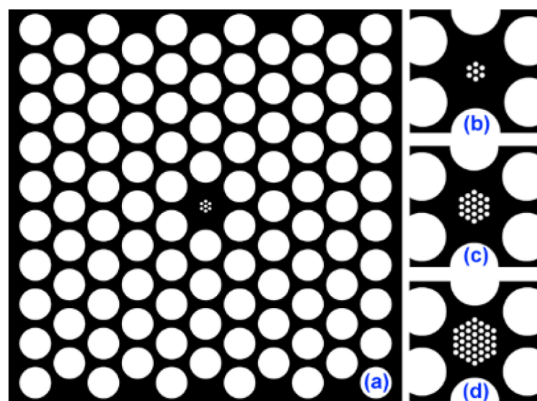
Generally speaking, extensive investigation has been done to induce point defects in PhCs as this results in defect modes, which give rise to many useful devices such as PhC fibers,<sup>228–230</sup> waveguides,<sup>231–234</sup> and defect-mode lasers.<sup>235–237</sup> Point defects have been investigated in several structures aside from 2D PhC slabs.<sup>238,239</sup> While literature concerning defects in PhCs is not extensive in the explicit case of gas-sensing capabilities, the principles behind the existing work extend to cases where defects were studied in more general applications.<sup>188,189,224,231,238–240</sup>

The effect of defects is often modeled *in silico* via finite-difference time-domain (FDTD) or finite element analysis in conjunction with analytical computation techniques such as the plane wave expansion method (PWEM).<sup>241,242</sup> In experimental applications, properties such as  $Q$ -factor, transmission spectra, and reflectance spectra are used to characterize defects. Kang and Weiss<sup>213</sup> investigated the use of MHDs in 2D PhCs as a replacement for point deletions. MHDs consisted of relatively small holes arranged in a hexagonal array, as depicted in Fig. 12. The MHD was found to introduce a high- $Q$  resonator functionality to the otherwise ideal 2D PhC slab. The presence of biomolecules in the MHD cavity alters the  $Q$ -factor of the cavity, which leads to its functionality as a biosensor. Compared with simple hole deletions, the MHD enables greater surface area for interaction between a target analyte and the PhC device, leading to better detection.

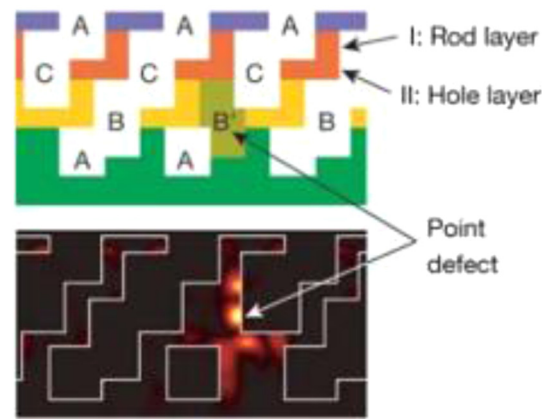




**Fig. 11** Example of spectral reflectance of a fabricated nanostructure post-exposure to a dry carrier gas (blank) and individual vapors, specifically water and methanol. (a)–(c) Spectra over different spectral ranges showing the responses to the blank, water vapors, and methanol vapors. (d) Response stability of a fabricated sensing nanostructure upon exposure to 160 cycles of methanol and water vapors over a time of 7.5 h. (e) Response reproducibility to 80 cycles of methanol and water. (f) Calibration curves for methanol and water. Figure modified from Ref. 8 and reprinted under the terms of the Creative Commons CC BY license.



**Fig. 12** Illustration of MHDs present in a hexagonal array of small holes, where (a) the dielectric constant plot of MHD simulation space is shown. Black indicates  $\epsilon = 12$ , while white indicates  $\epsilon = 1$ . MHD regions with effect radius (b)  $0.2a$ , (c)  $0.3a$ , and (d)  $0.4a$  are also provided. In (a)–(d), the defect hole radius in all cases is  $0.04a$  with a defect hole spacing of  $0.12a$ . Reprinted with permission from Ref. 213 © The Optical Society.



**Fig. 13** Schematic diagram (top) and image (bottom) showing the distribution of defects within the structure of the 3D PhC in the paper by Qi et al. Adapted from Ref. 212 and reprinted with permission through Copyright Clearance Center.

Point defects in 3D PhCs have also been explored.<sup>212,238,243</sup> Qi et al.<sup>212</sup> created point-defect microcavities, which resulted in defect mode localization around telecommunications wavelengths. Defects were introduced by occasionally over-etching the fabricated structure onto the previous layer, as seen in Fig. 13. Characterization of the resultant PhC using multiple angles of incidence showed a wide range of angles, which enabled the localization of resonant modes within the bandgap. The presence of analytes such as gases or biomolecules could be examined in this 3D system, possibly enabling the fast measurement of the  $Q$ -factor for resonant modes with low sensitivity to both angle of incidence and coupling efficiency.

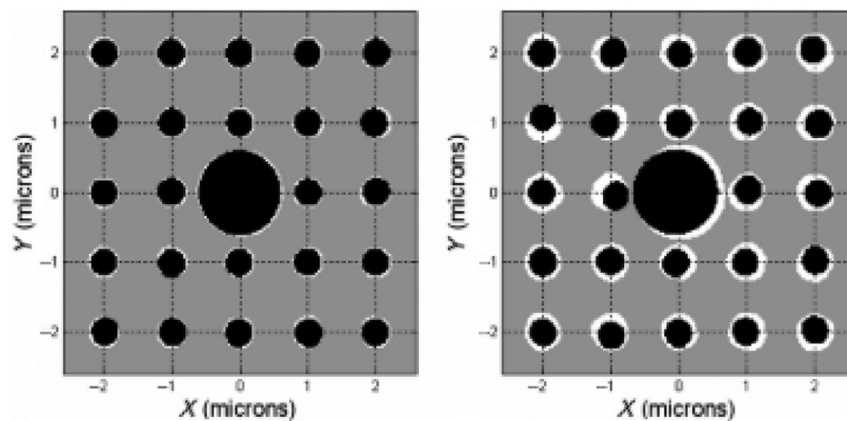
## 5.2 Impact of Disorder on Characterization of Photonic Materials

Random variation in the parameters of PhCs has been studied extensively in the past.<sup>223,244–246</sup> Generally, literature examples of this type of randomness use 2D PhC slabs to show the efficiency or characteristics of devices and optics, and then, the disorder is introduced.<sup>223,226</sup> Disorder has been shown to increase the angular tolerance of devices,<sup>247,248</sup> lower the intensity of resonant modes,<sup>249</sup> blueshift the resonant modes,<sup>222,250</sup> and introduce Anderson localization of light.<sup>188,246,251,252</sup>

In a study by Takeda et al.,<sup>246</sup> the introduction of randomness via air hole location was investigated for a 2D PhC slab with a triangular unit cell. The PhC slab had a single-hole deletion to introduce a defect mode within a complete TM bandgap. When randomness was introduced via a random number generator, the intensity of the defect mode was reduced, whereas high-intensity modes near the band edge were introduced. These modes were attributed to Anderson localization, which arises from coherent backscattering.

Topolancik et al.<sup>253</sup> investigated the effects of random disorder on the performance of a PhC waveguide by optically characterizing a sample fabricated with EB lithography. The waveguide was a 2D PhC slab consisting of a hexagonal unit cell composed of pentagonal air holes. Randomness was introduced by rotating the pentagonal air holes by 24 deg rather than by adjusting size or position. The orientation of a particular pentagon was random, but the number of pentagons oriented in the same direction was held constant. Anderson localization, which arises from the introduction of the random disorder, leads to the waveguide acting as a “random resonator” as described by the authors. This is similar to a designed nanocavity, but the introduced randomness enables an increase in  $Q$ -factor while limiting modal volume.

Other work has been done to show the tolerance of cavity resonators to disorder. A square unit cell was used by Rico-Garcia et al.<sup>254</sup> to make a rod-in-vacuum PhC slab consisting of a rod-expansion point defect, wherein a single rod’s radius was expanded, as seen in Fig. 14. Spatial dispersion of rods (including the point defect rod) was modulated randomly by adjusting parametric values of each rod. Rods were defined geometrically as ellipses, and adjusted parameters were  $x$ - and  $y$ -coordinates of rod centers, major and minor axes of the ellipses, and orientation of ellipses relative to the reference frame. Randomness was introduced at 1%, 3%,

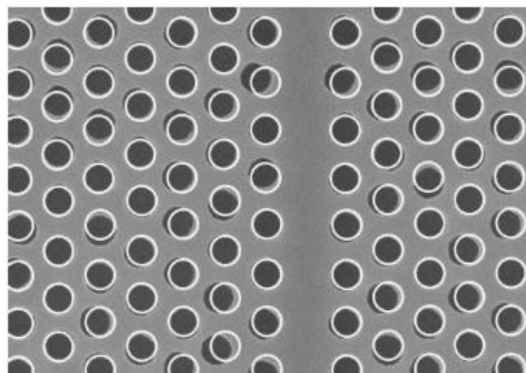


**Fig. 14** Geometry of a PhC microcavity. White outline surrounding the pillars corresponds with the distribution of possible locations of rods. Reprinted with permission from Ref. 254 © The Optical Society.

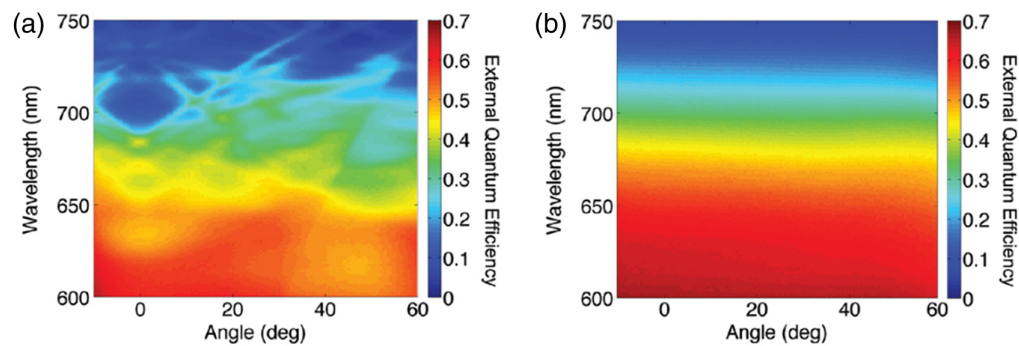
and 5% variation from a perfect PhC to simulate manufacturing error. The effects in the electromagnetic field for a microcavity were described as a function of the percent error of rod distribution, and it was found that errors of 1% to 5% do not appreciably disfigure the electromagnetic field distribution for a microcavity.

O'Faolain et al.<sup>255</sup> introduced pseudo-random air hole displacement into a W1 waveguide composed of a hole-in-dielectric system with a hexagonal unit cell, depicted in Fig. 15. A line deletion was performed for the PhC to function as a waveguide. FDTD (using RSOFT FULLWAVE, which can sample features smaller than the resolution grid) was used to characterize transmission and reflectance for the PhC. Band diagrams were made using PWEM via MPB. Reflectance and transmission losses were not greatly affected away from the band edge, but reflection loss was greatly increased near the band edge where the waveguide mode cutoff was. This was largely attributed to highly increased reflection near the band edge corresponding to a shift in the cutoff for the waveguide mode. The authors stated that the work shows the ability to use slow Bloch modes away from the cutoff point without having significant signal loss due to the effects of random disorder.

Disorder in media often increases the angular tolerance of light coupling into a structure.<sup>247,248,256</sup> Vynck et al.<sup>256</sup> showed that for thin film solar cells, the integration of a randomly textured surface enables broadband and wide-angle properties of disordered systems in conjunction with light trapping. Optimization of the wide-angle properties of disordered media has been explored by other groups as well,<sup>257–259</sup> giving a good database of random textures, which provide an isotropic angular response. To an extent, increasing the amount of disorder in a periodic structure increases coupling efficiency to an optical system, improving wave transport properties of optical devices, as seen from Ferry et al.<sup>258</sup> in Fig. 16.



**Fig. 15** Example of a disordered PhC waveguide used. White circles represent the locations of air holes for the ideal PhC equivalent. Figure taken from Ref. 255 © The Optical Society.



**Fig. 16** (a) External quantum efficiency of a PhC as a function of wavelength and angle of incidence for a periodic (b) and randomly nanotextured thin-film optical system. Figure adapted from Ref. 258. Copyright 2011 American Chemical Society.


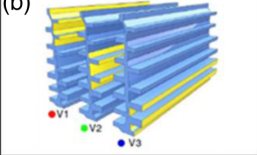
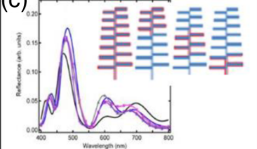
Disorders in tree-like structures and comparative analyses among long-, medium-, and short-range order have been studied.<sup>226</sup> Short-range disorder was determined to cause a peak in the reflectance spectrum, causing coloration, whereas long-range disorder gave a shiny, metallic-like appearance. This study can be directly compared with bio-inspired structures of similar degrees of disorder: the dorsal scales of *Cyanophrys remus* butterflies have long-range order, the ventral scales of *C. remus* butterflies have medium-range order, and scales from the *Albulina metallica* butterfly have short-range order. From these studies and based on the reflectance spectra predicted and observed from these structures, the relation of nanostructure and optical properties of different butterfly wing scales has been investigated and can be applied to other biological photonic systems, such as those observed in the structures of avian feather barbs and mammalian skin.<sup>226</sup>

## 6 Theoretical Studies of Photonic Materials

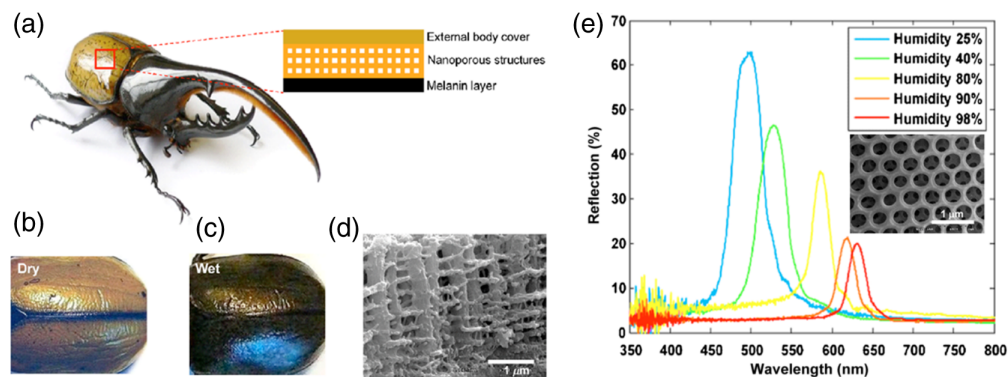
As of the writing of this article, only a few theoretical studies could be found in the literature that focused specifically on bio-inspired photonic structures for gas-sensing applications.<sup>7,8,218,260–263</sup> Among these, bio-inspiration appears to come in the form of either (1) structural<sup>8,218,260–263</sup> or (2) functional<sup>7</sup> mimicry. Sensors based on the *Morpho* butterfly, for example, are commonly comprised of structures that resemble a simplified version of the natural wing's "tree-like" nanostructure.<sup>8,218,260–263</sup> A humidity sensor inspired by the *Dynastes hercules* beetle,<sup>7</sup> on the other hand, takes on an inverse opal structure that is markedly different from the beetle's actual network of filamentary strings. In this case, the synthetic structure is made porous and hydrophilic, taking inspiration from the humidity-sensing mechanism of the natural structure. In the following sections, a brief review of theoretical studies is provided, which aided in characterizing photonic materials with varying morphologies, specifically those with porous and tree-like structures. We note that all the theoretical studies of photonic materials discussed below were concerned with performance in the visible wavelength range (320 to 800 nm). Nonlinear effects were not considered in these theoretical analyses presumably because the fields interacting with the analytes are expected to be of relatively low strength. Figure 17 summarizes the key methods of the studies discussed in this section.

### 6.1 Morphology of Porous Structures

Kim et al.<sup>7</sup> demonstrated a biomimetic humidity sensor inspired by the *D. hercules* tropical beetle [seen in Fig. 18(a)] in which analytical tools were used to study changes in refractive index as a function of humidity level. The beetle's elytra shifted visibly from a khaki-green when dry to a darker, nearly black color when exposed to high humidity [Figs. 18(b) and 18(c)]. The structural coloration arises from a 3D periodic structure residing in a porous layer beneath the cuticle surface.<sup>265,266</sup> The periodic structure resembled a "network of filamentary strings, arranged in layers parallel to the cuticle surface,"<sup>7</sup> which can be seen in Fig. 18(d). The porous layer contained nano-sized holes that are occupied by air when dry but filled with water as humidity

Photonic Structure	Theoretical Methods	Bio-Inspiration	Target Gases / Vapors	Applications
(a) 	Analytical, including Bragg's equation, to determine peak reflection wavelength.	Humidity-dependent color change of the Hercules beetle.	Water / humidity.	Humidity sensor in the visible wavelengths (e.g., meteorology, agriculture, medical equipment).
(b) 	Finite-element modeling and a custom Fresnel-based multilayer code.	Multivariable sensing capabilities of the <i>Morpho</i> butterfly.	Benzene, methyl ethyl ketone, acetonitrile, methanol, and water.	Chemical surveillance in public places, workplace monitoring using wearable sensors, monitoring in harsh environments.
(c) 	RCWA.	Chemical sensing properties of the <i>Morpho</i> butterfly.	DCP, DMMP, EtOH, MeOH, and water.	Sensing of chemical warfare agent vapors.

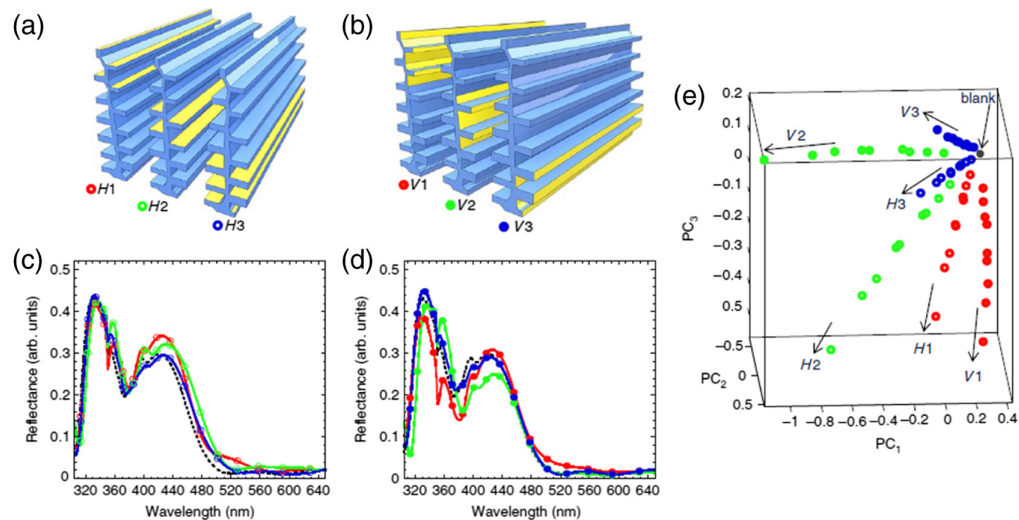
**Fig. 17** Summary of theoretical methods used for studies on bio-inspired photonic gas sensors. (a) Figure modified from Ref. 7 and reprinted with permission through Copyright Clearance Center. (b) Figure modified from Ref. 8 and reprinted under the terms of the Creative Commons CC BY license. (c) Figure adapted from Ref. 261 with permission from ACS Publications. The ACS article can be found at Ref. 264. Further permissions related to the material excerpted should be directed to the ACS.



**Fig. 18** (a)–(d) *D. hercules* beetle and its humidity sensing properties. (e) The reflection spectrum under a variety of humidity conditions. The inset shows the inverse opal structure of the fabricated humidity sensor. Figure modified from Ref. 7 and reprinted with permission through Copyright Clearance Center.

increases. The refractive index of water ( $n \approx 1.33$ ), being different than that of air ( $n \approx 1.0$ ), induces variation in the visible color.<sup>267</sup>

The synthetic mimic was fabricated as a hydrophilic inverse-opal structure. In this way, similar to the natural structure, the nano-sized pores would be filled with air under dry conditions and moisture under humid conditions. Experimental measurements of the reflection of the humidity sensor showed a high sensitivity to the environment humidity: the peak reflection shifted to longer wavelengths in the visible spectrum as the humidity increased [Fig. 18(e)]. Studied theoretically, Bragg's equation<sup>268</sup> for normal incidence,  $\lambda = 2dn_{\text{eff}}$ , can be used to approximate the peak reflection wavelength.<sup>7</sup> Using this equation,  $d$  accounts for the interlayer spacing of the structure and nano-hole diameter, and  $n_{\text{eff}}$  is the effective refractive index of the structure, which accounts for the nano-hole fill-factor and the surrounding media. The peak reflected wavelength shift when exposed to humidity is given by  $\Delta = 2d(n_{\text{eff}}^* - n_{\text{eff}})$ , where  $n_{\text{eff}}^*$  describes the effective refractive index under humid conditions.<sup>269</sup>



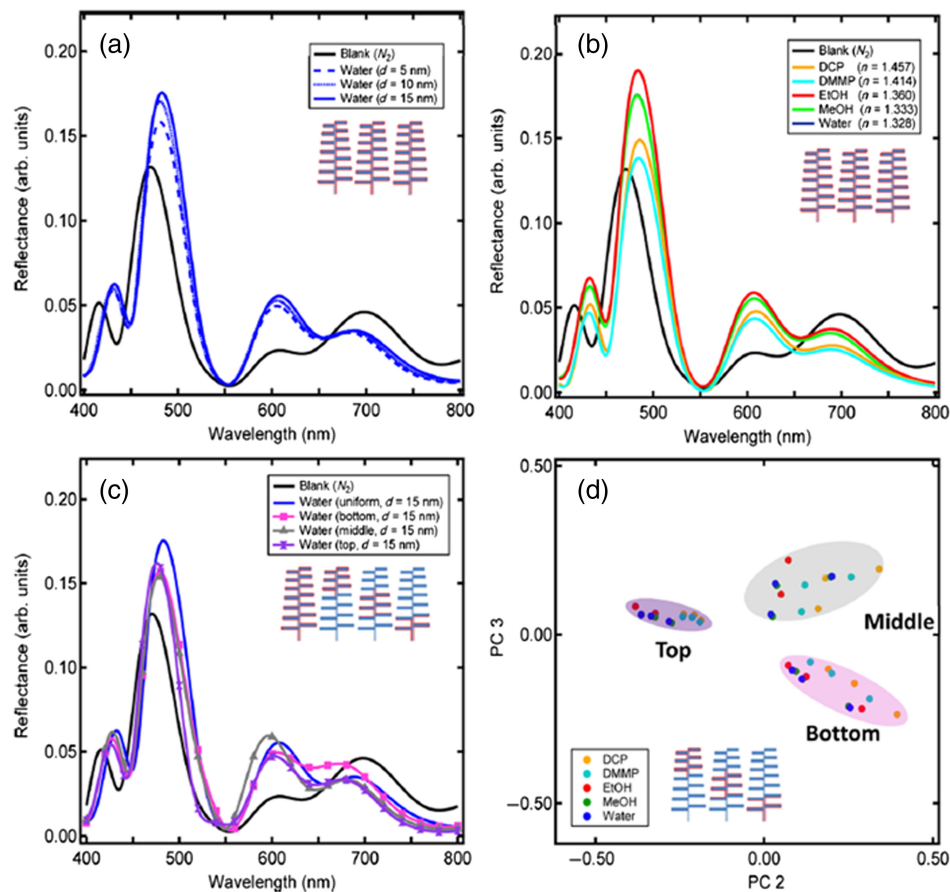
**Fig. 19** Finite-element simulation results by Potyraiilo et al. show that the location of vapor adsorption along the structure is important and can yield detectable differences in the reflection spectra. Adsorption onto (a), (c) horizontal surfaces of the lamellae yields different reflection properties than when adsorption occurs onto (b), (d) vertical surfaces. (e) PCA was used to distinguish between all configurations. This property can be used to design multivariable sensors, where a single structure can be used to detect multiple vapors. Figure modified from Ref. 8 and reprinted under the terms of the Creative Commons CC BY license.

## 6.2 Morphology of Tree-Like Structures

Potyraiilo et al.<sup>8</sup> used finite-element modeling to simulate light reflectance from *Morpho*-inspired photonic structures. The structures resembled a simplified version of the natural wing's tree-like nanostructure, depicted in Fig. 19(a), accounting for tapered and offset lamellae to realistically approximate the features of the natural structures.<sup>270</sup> With finite-element modeling, the group found that the location of vapor adsorption along the height of the structure can have a detectable impact on the resulting reflectance spectra. This selective adsorption mimicked the effect of a chemical functionalization gradient found in the natural structures, where different vapors could adsorb onto different locations along the structure.<sup>8,261</sup> This finding allowed for, in theory, a multivariable device in which appropriate chemical functionalization could be applied so that a variety of target vapors adsorb onto different regions of the same structure. This work modeled vapors as having refractive indices of  $n = 1.3, 1.4,$  and  $1.5$  and thicknesses  $d = 5, 10,$  and  $15$  nm relating to their gas-phase concentration-dependent thickness.<sup>271–273</sup> The current multivariable sensor designs were limited to sensitivity on the order of part-per-million. The authors note that this effort focused on selectivity, not sensitivity, enhancement. If enhancements to sensitivity are desired, there exist well-established design criteria, including increasing the number of lamellae, controlling the ridge-to-ridge spacing to introduce high-Q resonances in the reflectance spectra, and others.

Kittle et al.<sup>261</sup> used the rigorous coupled-wave analysis method<sup>274</sup> to investigate *Morpho*-inspired nanostructures and the impact of vapor concentration, refractive index, and adsorption location on their resulting spectra. They found that all three parameters had a detectable impact on the reflection spectra, shown in Fig. 20. The vapor concentration was modeled as an effective thickness [Fig. 20(a)]. Distinct vapors were assigned an effective refractive index [Fig. 20(b)] where differences in the spectra were evident even with vapors of similar refractive indices. Finally, vapor location was varied by only applying a non-air conformal layer to select regions of the structure [Fig. 20(c)]. Principal component analysis (PCA)<sup>275</sup> [Fig. 20(d)] showed that the responses due to distinct vapor locations could be isolated, potentially enabling multivariable sensing characteristics.

This study was concerned with the sensing of chemical warfare agent simulants, including dimethyl methylphosphonate, a nerve agent simulant, and dichloropentane, a mustard gas simulant. The LOD from tests with an actual butterfly wing were on the order of parts-per-million. The authors note that synthetic mimics must improve on these sensitivities for practical use.



**Fig. 20** Simulated reflection spectra of *Morpho*-inspired nanostructures investigating the impact of (a) vapor concentration, (b) vapor refractive index, and (c) vapor location along the structure, in which (d) PCA can help isolate the responses from distinct locations. Figure adapted from Ref. 261 with permission from ACS Publications. The ACS article can be found at Ref. 264. Further permissions related to the material excerpted should be directed to the ACS.

The nerve agent VX, for example, can be lethal at concentrations of as little as 0.3 ppm. The authors further provided design guidelines to help increase sensor sensitivity, including careful selection of the refractive index, optimized periodicity, and targeted functionalization of certain regions within the PhC.

In most *Morpho*-butterfly-inspired models, the refractive index is defined as having  $n = 1.56$  and  $\kappa = 0.068$ .<sup>276</sup> The loss component, although relatively small, has been reported as especially impactful in providing diversity in the spectral response. Potyrai et al.,<sup>8</sup> for example, found that the “selectivity of the sensor was strongly dependent on the extinction coefficient  $\kappa$  of the lamellae.”

## 7 Characterization and Function of Plasmonic Sensors

Plasmonic nanoparticles exhibit exciting properties such as scattering,<sup>277</sup> absorbance,<sup>278</sup> and coupling (electrons oscillate at the same frequency as the light) based on their geometrical size and shape, composition, relative positions, and local dielectric environment.<sup>279,280</sup> It is possible to increase the performance of an optical gas sensor through plasmonic effects.<sup>8,217,218,219</sup>

*Morpho* butterfly wings have been explored as photonic structures for gas, vapor, IR, and temperature sensor applications.<sup>145,281</sup> Pris et al.<sup>282</sup> first demonstrated that the butterfly wings were doped with single-walled nanotubes (SWNTs) to boost the absorption of IR photons. The IR radiation was absorbed and converted into heat, and the temperature of the wing structure increased. As a result, the nanostructures of the wings expanded and changed the reflectance in the visible wavelength. Combining the low-thermal mass of the air-filled wing nanostructures

with the good IR absorption by the doped SWNTs enabled this system to perform as a high-speed IR sensor with a temperature sensitivity of 62 mK and a heat-sink-free response speed of 35 to 40 Hz. The spacing change between ridges upon thermal expansion under IR radiation played a significant role in the high sensitivity of the IR response. By contrast, the expansion of the lamella and reduction in the refractive index only played minor roles in the IR response from such sensor design.

Zhang et al.<sup>190</sup> developed a butterfly wing-based IR sensing approach in which they selectively modified the butterfly wing structure to achieve a pseudo-3D bimorph structure. The edge of the lamella was coated with Au through PVD. Due to the difference in the coefficient of thermal expansion between the chitin of the wings and the Au coated on top of the wings, the absorption of the IR radiation would cause the temperature increase and subsequent bending of the lamella. This bending effect resembles the photo-mechanic deformation of the artificial bio-morph structures used for IR detection. The structural deformation on each lamella during the IR absorption changed the optical property. This change from all the lamellae arranged in 3D resulted in enhanced sensitivity for IR stimulation. The design achieved a temperature sensitivity of 32 mK, a twofold increase over the butterfly wings doped with SWNTs.

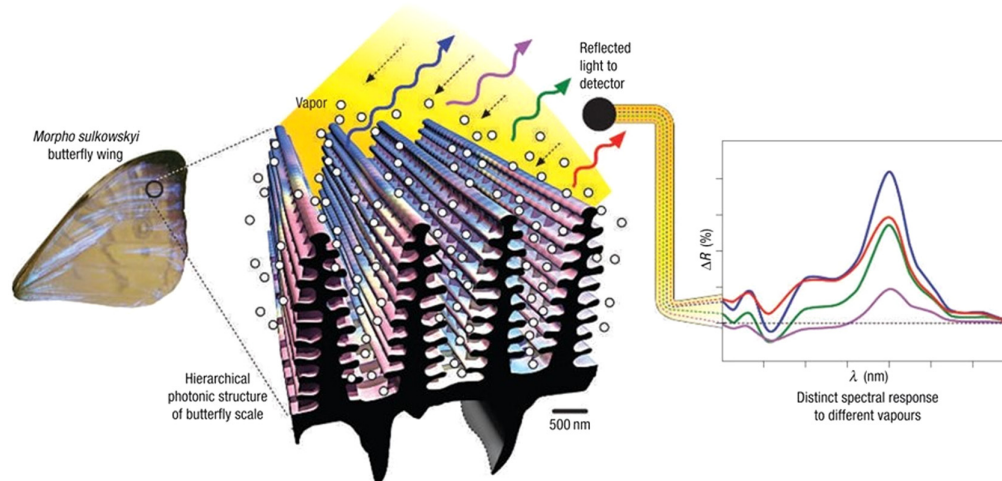
Other temperature-sensitive results were previously reported on similar structures. For instance, Lu et al.<sup>283</sup> reported a bioinspired thermo-responsive photonic structure obtained by attaching thermo-sensitive poly(*N*-isopropylacrylamide) (PNIPAM) to the surface of a *Morpho* butterfly wing using glutaraldehyde. The PNIPAM-modified butterfly wing exhibited a reversible reflection spectra shift as a function of temperature change. In addition, Xu et al.<sup>284</sup> used PNIPAM-based material and poly(*N*-isopropylacrylamide)-co-acrylic acid (PNIPAM-co-AAc) to achieve sensitive thermal detection with optical readout. The *Morpho* butterfly–PNIPAM hybrid material had a red shift in the wavelength when the temperature increased because PNIPAM's refractive index changed with temperature. The *Morpho* butterfly–(PNIPAM-co-AAc) system showed a blue shift with the increase in the temperature due to the change in the thickness of the PNIPAM-co-AAc coating.

Hybrid thermo-responsive structures can also be used for IR sensing applications due to their sensitive response to temperature changes. Due to the IR absorbance of the PNIPAM-based material and butterfly wing itself, the nanostructures on the wings will deform upon IR illumination.<sup>285</sup> As a result, it causes the blue or red shift of reflectance spectra for the optical readout. It might be possible to further improve IR sensing abilities by optimizing the thickness of the PNIPAM on the wing surface. This could be done by tuning the sensitivity range through chemical modification.

Selective response to diverse vapors makes butterfly-wing structures potentially useful for gas sensor applications.<sup>6</sup> Potyrailo et al.<sup>218</sup> found that a single photonic structure had various differential reflectance spectra with different vapors and highly selective responses to individual vapors. The critical analysis of the data suggested that the optical response is mainly due to a combination of physical adsorption and capillary condensation of gas molecules in the gaps of the lamellae. In 2014, Jiang et al.<sup>263</sup> identified nitrogen, methanol, and ethanol vapors using *Morpho* butterfly-wing structures. This detection was achieved by the PCA method based on the masses of collected spectral data. In 2013, Potyrailo et al.<sup>217</sup> discovered the presence of a polarity gradient on the *Morpho* butterfly scales surface. Once the *Morpho* scales were exposed to vapors and gas molecules, a scale with a high polarity gradient gave a strong reflection peak at the visible wavelength. Furthermore, it was concluded that the spectral change was caused by the change in lamella thickness and refractive index because there was a thin layer of vapors and gas molecules present on the structure's surface, depicted in Fig. 21.<sup>8</sup>

Subtractive modification using oxygen plasma etching has been shown to change the properties of butterfly wings.<sup>286,287</sup> Shen et al.<sup>286</sup> reported that butterfly wings could be controllably modified using oxygen plasma etching. This caused observed changes gradually in the optical properties, which allowed for a better understanding of the properties of the structure, which evolved through natural evolution. The primary material of the butterfly wings is chitin, and oxygen molecules ( $O_3$ ) were excited to generate active ions ( $O^{3+}$ ,  $O^+$ ,  $O^-$ ). These highly active ions would react with the organic molecules, primarily chitin, at the surface of the wings. The reactions lead to the generation of  $H_2O$ ,  $CO$ ,  $CO_2$ , and hydrocarbons with lower molecular weight. These volatile molecules could be subsequently removed via vacuum pumping during





**Fig. 21** Schematic diagram of how highly selective vapors respond based on hierarchical photonic structures, demonstrated using *M. sulkowskyi* iridescent scales. Measurements of differential reflectance spectra  $\Delta R$  can provide information about the nature and concentration of vapors present. Figure taken from Ref. 218 and reprinted with permission through Copyright Clearance Center.

the etching process. The hierarchical nanostructures of the wings were controlled by varying the reaction time in a subtractive manner. The thickness of lamella layers on each ridge of the wings was reduced during the initial etching process. With a longer etching time, the number of lamella layers was also reduced. Such subtractive modification not only shifted the wavelength of the reflectance peak and reduced the reflectance of the wing scales but also helped understand the view-angle independent property of the wings. Piszter et al.<sup>191</sup> investigated the interaction between the chitin nanoarchitecture and the volatile vapors. *P. icarus* was coated with 5 nm  $\text{Al}_2\text{O}_3$  and was used to detect seven volatiles. Reduced sensitivity and selectivity were observed when the chitin was isolated from the vapors. A reversible chemical interaction caused swelling, which occurred between the sample and the volatiles in the pristine wings. The capillary condensation of the vapors into the nanoarchitecture became dominant for acetone, ethanol, chloroform, toluene at higher concentrations, and isopropanol at low concentrations. Potyrailo et al.<sup>288</sup> developed a multivariable electrical resonant sensor, built a wireless sensor node, and connected the system to a cloud server for data upload and analytics. The sensor was tuned for the detection of  $\text{CH}_4$  in underground mines and provided rejection of interferences in ambient air such as moisture and fumes of diesel-operated equipment. The autonomous node with the sensor was exposed to  $\text{CH}_4$  and high concentrations of water vapor and toluene vapor. Principal components described orthogonal outputs generated by the sensor upon multivariate data analysis. Higher dispersion levels allowed for more accurate quantitation of multiple analytes and enhanced sensor stability. Tests with vapors of diverse nature were performed using benzene, methyl ethyl ketone, acetonitrile, methanol, and water, producing distinctly different reflectance spectra for each vapor.

In the presence of interferences, gas sensor performance often degrades in the field.<sup>58</sup> This necessitates new sensing approaches with improved selectivity. Potyrailo et al.<sup>289</sup> recently boosted and optimized the sensor's performance using machine learning. Catalytic metal nanoparticles (5 to 50 nm in diameter) and metal oxide capping layers on nanoparticles were used to promote reactions with the gases of interest. The results reported in this study for  $\text{H}_2$  and CO analyte gases were achieved using fabricated inorganic nanostructures with variable-size catalytic metal nanoparticles capped with a  $\text{CeO}_2$  layer. Water, chloroform, and dimethylformamide were the three vapor sources used in this experiment. The vapors' exposure angles were 20, 40, and 60 deg measured from the normal to the nanostructure surface. At a small illumination angle of 20 deg, the  $\Delta R(\lambda)$ -spectra of the three vapors were very similar, with the differences in  $\Delta R(\lambda)$ -spectra becoming more significant at 40 and 60 deg. The PCA scores plot showed two interesting features for a more quantitative interpretation. First, the angular spread between the response

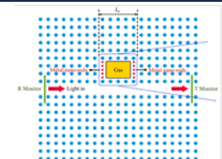
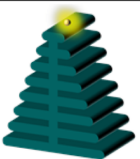
directions of the same sensing nanostructure to three vapors increased as the exposure angle increased. Second, the relative magnitudes of the responses decreased as the exposure angle increased. For  $H_2$  and CO sensing for solid oxide fuel cell applications, 3D nanostructures were fabricated with a ridge of  $SiN_x$  material, lamellae of  $SiO_2$  material, and Au nanoparticles embedded between the base and capping ceria layers.<sup>290,291</sup> These tests aimed to evaluate the response diversity of the nanostructures to  $H_2$  and CO gases and assessed the linearity of the response to  $H_2$  and CO. It is significant to note that the Au nanoparticles had a noticeable effect on the observed spectra. The plasmonic signature of the nanostructure was observed between 640 and 720 nm. The length of the lamellae was increased and decorated with AuNPs of different sizes to optimize the nanostructure design. This geometry enhanced the response magnitude and the discrimination between  $H_2$  and CO under different test conditions. The dynamic response of the nanostructure at 950 nm upon exposure to five gases ( $H_2$ , CO,  $CH_4$ ,  $CO_2$ , and  $H_2O$ ) with three replicates was investigated. The responses to  $H_2$  and CO were always at least two to three times stronger versus  $CH_4$ ,  $CO_2$ , and  $H_2O$ .

While not studied for gas-sensing applications, Ke et al.<sup>292</sup> reported interesting findings in which plasmonic  $VO_2$  nanoparticle coatings, bio-inspired by cephalopod skin, exhibited temperature-dependent localized surface plasmon resonance where micro-wrinkles were present. Simulations of wrinkle formation were done using ABAQUS software. With a fixed solar energy modulation implemented, visible transmittance from 60% to 17% could be controlled as a result of tuning the wrinkles to induce diffraction. These changes in optical properties could be beneficial to advancing our understanding of optical properties for gas sensors.

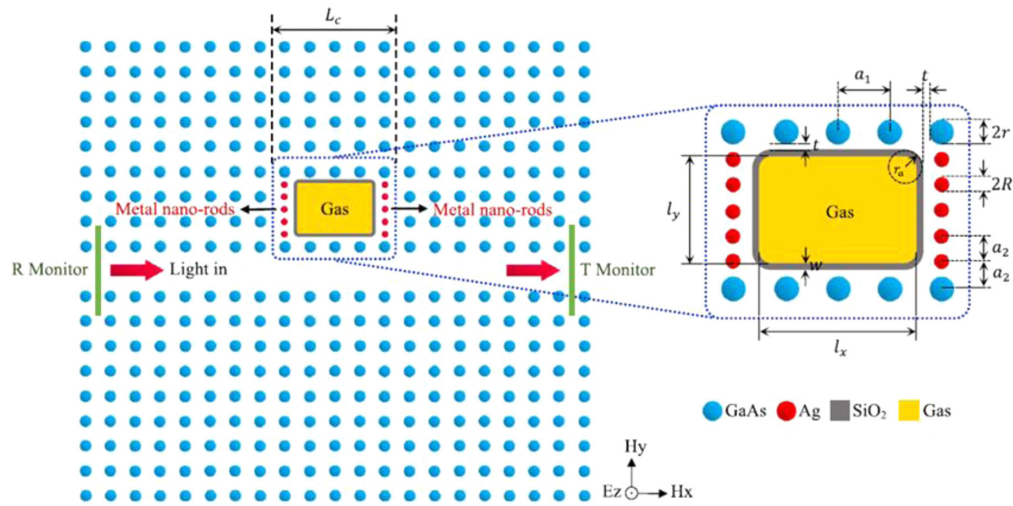
## 8 Theoretical Studies on Plasmonic Materials

To date, no examples could be found in the literature of theoretical studies on (1) bioinspired (2) plasmonic-enhanced PhC structures (3) as applied to gas/chemical vapor sensing. The studies discussed below are included because they are either bioinspired or used, or can be used in principle, as a gas sensor. Nonlinear effects were not considered in these theoretical analyses presumably because the fields interacting with the analytes are expected to be of relatively low strength. Figure 22 summarizes the key methods of the studies discussed in this section.

Hajshahvaladi et al.<sup>293</sup> devised a hybrid plasmonic-PhC based on a square lattice of GaAs ( $n = 1.34$ ) rods with a one-row-defect bandgap waveguide configuration for gas-sensing applications in the NIR (1500 to 2100 nm). Near the row defect, several rods were removed to create a small cavity surrounded by a thin  $SiO_2$  layer where the gas would reside. The purpose of the  $SiO_2$  layer was to contain the gas within the cavity and prevent it from bleeding into the PhC, where the background permittivity would be changed and the PhC optical properties modified. Silver nanorods were added to two sides of this cavity to provide plasmonic enhancement. Figure 23 shows the conceptual setup and mode of operation.

Photonic–Plasmonic Structure	Theoretical Methods	Bio-Inspiration	Target Gases / Vapors	Applications
	FDTD.	N/A.	$NH_3$ , $Cl_2$ , $Br_2$ .	Highly sensitive and high-resolution sensing applications.
	FDTD.	<i>Morpho</i> butterfly wing.	N/A.	SERS, enhancements to localized electric fields.

**Fig. 22** Summary of the theoretical methods used for studies on bio-inspired photonic–plasmonic gas sensors. Figure modified from Ref. 293 and reprinted with permission through Copyright Clearance Center.

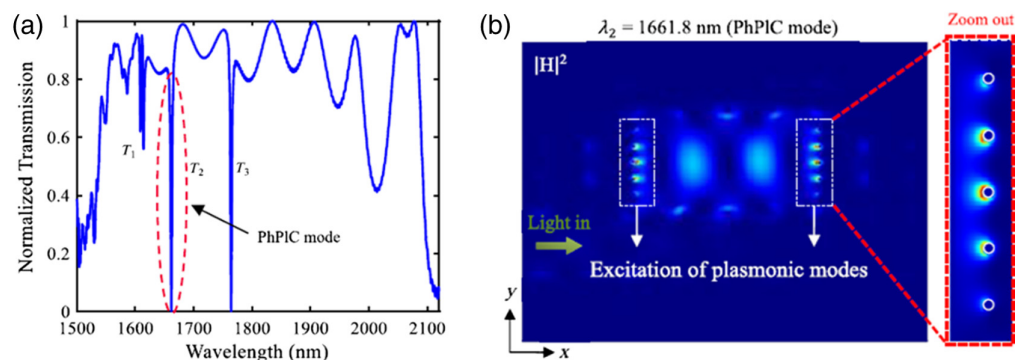


**Fig. 23** 2D schematic of a hybrid PhPIC sensor device. Figure taken from Ref. 293 and reprinted with permission through Copyright Clearance Center.

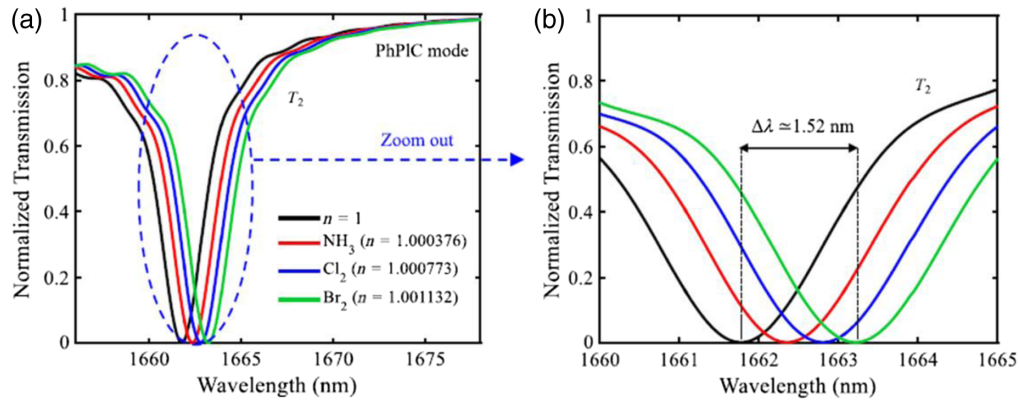
The operating principle of this device is based on the coupling of cavity and plasmonic resonances to strengthen the light–gas interaction.<sup>294</sup> Figure 24(a) shows the transmission response of the hybrid photonic–plasmonic crystal (PhPIC). Three transmission dips are labeled  $T_1$ ,  $T_2$ , and  $T_3$ , where  $T_2$  is identified as a PhPIC mode arising from plasmonic resonances from the Ag nano-rods. A snapshot of the magnetic field distributions at  $T_2$  [Fig. 24(b)] validates that this resonance indeed arises from the metal rods. This resonance condition is desired because it produces a stronger light–gas interaction within the cavity, which is a property that can improve sensor performance.<sup>295</sup>

The device was modeled under exposure to  $\text{NH}_3$ , chlorine ( $\text{Cl}_2$ ), and bromine ( $\text{Br}_2$ ) gases, all of which can be harmful to humans and the environment.<sup>296</sup> Simulating the transmission spectra for these different gases shows that there is a resonance wavelength shift that depends on the gas refractive index (Fig. 25). The authors note that this photonic–plasmonic mode ( $T_2$ ) can be approximated as a linear relationship between the resonance wavelength and the gas refractive index of the system as  $\lambda = 975n + 789.1$ . Comparing this result to the pure PhC response of  $T_3$ , it is noted that the wavelength shifts of the hybrid PhPIC system are more pronounced, offering better sensor performance.

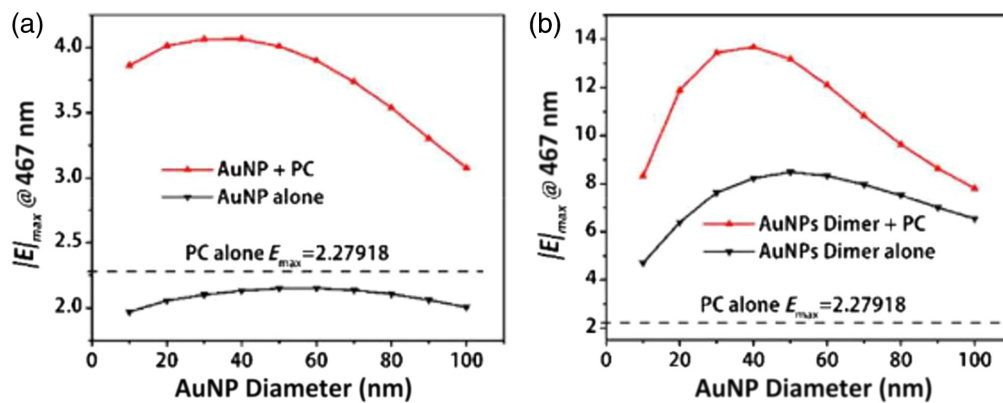
The group used the FDTD method to perform these simulations.<sup>297</sup> The spatial discretization step was set to 5 nm, and the frequencies of interest were 1500 to 2200 nm. The authors noted that for a 2D simplification to be valid, the height of the rods should be much larger than the input wavelength.<sup>298,299</sup> Considering a rod height of 2  $\mu\text{m}$ , the authors commented that the height is large enough to not invalidate 2D results and is therefore a good approximation to 3D results.



**Fig. 24** (a) Normalized transmission spectrum of the hybrid PhPIC. (b) The magnetic field distribution at  $T_2$  confirms that this resonance arose from the Ag rods. Figure adapted from Ref. 293 and reprinted with permission through Copyright Clearance Center.



**Fig. 25** Simulated transmission spectra of the hybrid PhPIC sensor exposed to different gases. (a) the resonance wavelength of T2 (b) a “zoomed” perspective. Figure adapted from Ref. 293 and reprinted with permission through Copyright Clearance Center.



**Fig. 26** Optimization study to maximize the electric field enhancement as a function of nanoparticle diameter. (a) The peak  $|E|$ -field is compared with the PhC alone, the Au nanoparticle alone, and a combination of the two. (b) The peak  $|E|$ -field is again compared with the PhC alone, the Au nanoparticle dimer alone, and a combination of the two. Figure adapted from Ref. 301 with permission from The Royal Society of Chemistry.

The PWEM was then used to calculate the band diagrams for the baseline PhC (i.e., without plasmonic enhancements).<sup>242</sup> To define the refractive index of Ag, the group used the often-cited experimental dataset by Johnson and Christy.<sup>300</sup>

Mu et al.<sup>301</sup> modeled bioinspired PhCs with a plasmonic enhancement via an AuNP dimer but not explicitly for their gas-sensing capabilities. Instead, the device was studied for its field enhancement properties in the visible range (400 to 700 nm). The group performed an optimization study to determine the required AuNP dimer spacing, location, orientation, and number of lamellae to maximize the field enhancement.<sup>302,303</sup> AuNP and AuNP dimer diameters were also varied to maximize the field enhancement with and without the PhC, shown in Fig. 26. Their simulations clearly show that the addition of AuNPs and AuNP dimers can provide plasmonic enhancements that contribute to overall field enhancements. These field enhancement properties were discussed as being potentially useful in SERS.<sup>304</sup>

## 9 Conclusions and Outlook

In summary, a comprehensive review of bio-inspired photonic and plasmonic materials has been provided from fabrication, experimental, and theoretical perspectives for gas-sensing applications. Fabrication of photonic nanostructures and coatings for plasmonic effects has been reviewed extensively, with a variety of methods discussed. Fabrication of photonic nanostructures has been demonstrated using a variety of top-down methods, such as the traditional EBL, photolithography, and nanoimprint lithography. Improvements in IL have allowed researchers to

create structures with unique topologies, which deviate from usual periodic, isotropic patterns. Self-assembly techniques such as vertical deposition, dip-coating, and colloidal self-assembly enable the creation of PhCs from block copolymer or nanoparticle solutions, which show promise as gas sensors. Thin films can be applied to fabricated nanostructures and PhCs by physical vapor or CVD methods. These additional coatings widen the design space through modification of the sensor response. These fabrication methods can be ultimately used to develop photonic and plasmonic materials for gas-sensing applications.

Experimentally, gas-sensing applications of bio-inspired nanoparticles, fiber optic systems, porous materials, and tree-like structures have been explored extensively. Photonic materials fabricated with various morphological differences allow for changes in the observation of a modulated optical response upon the introduction of an analyte gas. The allowed modes of propagation within a PhC are altered, which affects the transmission spectrum of output light from the photonic material. The transmission spectrum can be used not only to detect the presence of gas but also to calculate the gas concentration within the structure. In addition, PhC fibers have the capability to detect the presence of complex molecules such as DNA.

Specific to bio-inspired tree-like pillars fabricated based on *Morpho*-butterfly nanostructures, the sensitivity, selectivity, dynamic response, and midwave IR detection capabilities can be modified based on morphological changes and can be utilized for gas-sensing applications. The spacing between lamellae changes due to thermal expansion, which results in a change in reflectivity. The temperature sensitivity could be enhanced by increasing the difference between the expansion coefficients of the deposited material and the chitin, as well as by optimizing the thickness of the deposited material. Smart polymers can be co-assembled with bio-hierarchical structures to obtain ideal stimuli-responsive photonic structures. Selective responses to diverse vapors make butterfly-wing structures potentially useful for gas sensor applications. Physical adsorption and capillary condensation of gas molecules occur in lamellar gaps, which causes a change in lamella thickness and refractive index and results in a change in the optical spectrum. In the presence of interferences, gas sensor performance often degrades in the field. Machine learning tools allow the analysis of multivariate data and the relation of the weighted outputs to the concentrations of one or more gaseous species of interest. The reactions with the gas of interest can be facilitated by catalytic metal nanoparticles and metal-oxide capping on their surface.

PhCs have also been shown to be practical devices for gas sensing based on localized defects and long-range disorder. When PhCs have a break from perfect symmetry, the observed optical response can be greatly different from that of a perfectly ordered crystal. Gas-sensing capabilities often arise from the introduction of localized defects such as feature deletions and substitutions. Meanwhile, the addition of disorder across the entire PhC often changes the tolerance and sensitivity of the gas sensor created with localized defects. The deliberate introduction of local defects and systemic disorder allows for the rough design and fine adjustment of a PhC-based gas sensor.

While bio-inspired coatings with plasmonic effects have been studied with less abundance than photonic nanostructures for gas-sensing applications, experimental studies have shown a change in optical response, which is largely dependent on the diffraction of light from wrinkles on films and the presence of coatings. Plasmonic nanoparticles coated on substrates and even photonic nanostructures have been shown to enhance the optical responses observed as a result of their geometrical size and shape, as well as the local dielectric environment.

Theoretical studies centered around photonic and plasmonic materials that are both bio-inspired and conducted for gas-sensing applications are scarce in the literature. However, a review of theoretical studies was provided that aids in characterizing bio-inspired photonic materials from a computational standpoint. While no work has been previously reported in the literature for theoretical studies done on bio-inspired plasmonic materials for gas-sensing applications, some reports have been published within the scope of this work that could be referenced in efforts to facilitate the advancements of computational study within this field.

---

## Disclosures

The authors have no conflicts of interest to declare. All co-authors have seen and agree with the contents of this review.

## Code and Data Availability

The figures and data in this review were reprinted or adapted, with permissions, from their respective journals and through Copyright Clearance Center. All figures have been properly cited in the figure captions. Further permissions related to the material should be directed to the appropriate journal.

## Acknowledgments

This effort was partly supported by the Air Force Research Laboratory (AFRL) program (Grant No. FA8651-19-P-0110) and the Small Business Innovation Research (SBIR) program (Grant No. FA8649-20-C-0316). The authors also acknowledge support from the AFRL Scholars Program.

## References

1. S. Tadepalli et al., “Bio-optics and bio-inspired optical materials,” *Chem. Rev.* **117**(20), 12705–12763 (2017).
2. R. A. Potyrailo, “Toward high value sensing: monolayer-protected metal nanoparticles in multivariable gas and vapor sensors,” *Chem. Soc. Rev.* **46**(17), 5311–5346 (2017).
3. I. Abdulhalim, M. Zourob, and A. Lakhtakia, “Surface plasmon resonance for biosensing: a mini-review,” *Electromagnetics* **28**(3), 214–242 (2008).
4. H. Xu et al., “Photonic crystal for gas sensing,” *J. Mater. Chem. C* **1**(38), 6087–6098 (2013).
5. R. Potyrailo and R. R. Naik, “Bionanomaterials and bioinspired nanostructures for selective vapor sensing,” *Annu. Rev. Mater. Res.* **43**, 307–334 (2013).
6. M. I. Osotsi et al., “Butterfly wing architectures inspire sensor and energy applications,” *Natl. Sci. Rev.* **8**(3), 1–22 (2021).
7. J. H. Kim et al., “Biologically inspired humidity sensor based on three-dimensional photonic crystals,” *Appl. Phys. Lett.* **97**(10), 103701 (2010).
8. R. A. Potyrailo et al., “Towards outperforming conventional sensor arrays with fabricated individual photonic vapour sensors inspired by *Morpho* butterflies,” *Nat. Commun.* **6**(1), 7959 (2015).
9. Y. Bao et al., “Detection of volatile-organic-compounds (VOCs) in solution using cantilever-based gas sensors,” *Talanta* **182**, 148–155 (2018).
10. S. A. Taya et al., “Detection of harmful chemical compounds in plastic products using a high-sensitivity photonic crystal-based sensor,” *Phys. Status Solidi A* **220**(20), 2300547 (2023).
11. P. R. Gifford and S. Bruckenstein, “Pneumatoamperometric determination of parts-per-billion dissolved species by gas evolving reactions,” *Anal. Chem.* **52**(7), 1024–1028 (1980).
12. C. Tiebe et al., “Investigation of gaseous metabolites from moulds by ion mobility spectrometry (IMS) and gas chromatography-mass spectrometry (GC-MS),” *Int. J. Ion Mobil. Spectrom.* **13**(1), 17–24 (2010).
13. L. Palcsu et al., “Detection of tritium and alpha decaying radionuclides in L/ILW by measurements of helium isotopes,” *J. Radioanal. Nucl. Chem.* **286**(2), 483–487 (2010).
14. J. Soltani-Nabipour, A. Khorshidi, and F. Sadeghi, “Constructing environmental radon gas detector and measuring concentration in residential buildings,” *Phys. Part. Nucl. Lett.* **16**, 789–795 (2019).
15. C. R. Carrigan et al., “Trace gas emissions on geological faults as indicators of underground nuclear testing,” *Nature* **382**(6591), 528–531 (1996).
16. M. Schoepfner and A. Glaser, “Present and future potential of Krypton-85 for the detection of clandestine reprocessing plants for treaty verification,” *J. Environ. Radioact.* **162–163**, 300–309 (2016).
17. M. Wachsmuth et al., “On-line gas-phase separation of short-lived bromine nuclides from precursor selenium,” *Radiochim. Acta* **88**(12), 873–878 (2000).
18. B. H. Hamling and G. F. Jenkins, “Disposal of gaseous effluents from nuclear power plants,” *J. Air Pollut. Control Assoc.* **7**(4), 256–261 (1958).
19. N. U. Khattak et al., “Radon monitoring for geological exploration: a review,” *J. Himal. Earth Sci.* **44**(2), 91–102 (2011).
20. F. S. Olise, D. M. Akinagbe, and O. S. Olasogba, “Radionuclides and radon levels in soil and ground water from solid minerals-hosted area, South-Western Nigeria,” *Cogent. Environ. Sci.* **2**(1), 1142344 (2016).
21. L. J. Small, M. E. Schindelholz, and T. M. Nenoff, “Hold on tight: MOF-based irreversible gas sensors,” *Ind. Eng. Chem. Res.* **60**(21), 7998–8006 (2021).
22. C. Poinssot and H. Geckeis, *Radionuclide Behaviour in the Natural Environment: Science, Implications and Lessons for the Nuclear Industry*, Elsevier (2012).
23. G. W. Phillips, D. J. Nagel, and T. Coffey, *A Primer on the Detection of Nuclear and Radiological Weapons*, National Defense University Center for Technology and National Security Policy, Washington, DC (2005).
24. J. W. Gardner and J. Yinon, “Staff view: electronic noses & sensors for the detection of explosives,” <https://catalog.lib.uchicago.edu/vufind/Record/5548597/Details> (accessed 26 May 2023).

25. B. Firtat et al., “Miniaturised MOX based sensors for pollutant and explosive gases detection,” *Sens. Actuators B Chem.* **249**, 647–655 (2017).
26. M. J. Lefferts and M. R. Castell, “Vapour sensing of explosive materials,” *Anal. Methods* **7**(21), 9005–9017 (2015).
27. W. J. Peveler et al., “Detection of explosive markers using zeolite modified gas sensors,” *J. Mater. Chem. A* **1**(7), 2613–2620 (2013).
28. S. Khanniche et al., “Quantitative evaluation of the responses of a gravimetric gas sensor based on mesoporous functionalized silica: application to 2, 4-DNT and TNT detection,” *Sens. Actuators B Chem.* **248**, 470–480 (2017).
29. A. Ghoorchian and N. Alizadeh, “Chemiresistor gas sensor based on sulfonated dye-doped modified conducting polypyrrole film for high sensitive detection of 2, 4, 6-trinitrotoluene in air,” *Sens. Actuators B Chem.* **255**, 826–835 (2018).
30. T. Puttasakul et al., “Hydrogel based-electrochemical gas sensor for explosive material detection,” *IEEE Sens. J.* **19**(19), 8556–8562 (2019).
31. D. Gopalakrishnan and W. R. Dichtel, “Direct detection of RDX vapor using a conjugated polymer network,” *J. Am. Chem. Soc.* **135**(22), 8357–8362 (2013).
32. T. Kurita-Ochiai, K. Fukushima, and K. Ochiai, “Volatile fatty acids, metabolic by-products of periodontopathic bacteria, inhibit lymphocyte proliferation and cytokine production,” *J. Dent. Res.* **74**(7), 1367–1373 (1995).
33. M. Pimentel, R. Mathur, and C. Chang, “Gas and the microbiome,” *Curr. Gastroenterol. Rep.* **15**, 1–6 (2013).
34. G. I. Balali et al., “Microbial contamination, an increasing threat to the consumption of fresh fruits and vegetables in today’s world,” *Int. J. Microbiol.* **2020**, 3029295 (2020).
35. B. J. Umber et al., “Gas signatures from *Escherichia coli* and *Escherichia coli*-inoculated human whole blood,” *Clin. Transl. Med.* **2**, 13 (2013).
36. R. S. Oremland, L. M. Marsh, and S. Polcin, “Methane production and simultaneous sulphate reduction in anoxic, salt marsh sediments,” *Nature* **296**(5853), 143–145 (1982).
37. PubMed, “Detection of herpesviruses and periodontal pathogens in subgingival plaque of patients with chronic periodontitis, generalized aggressive periodontitis, or gingivitis,” <https://pubmed.ncbi.nlm.nih.gov/19053922/> (accessed 26 May 2023).
38. ACS Central Science, “Discovery of volatile biomarkers of Parkinson’s disease from sebum,” <https://pubs.acs.org/doi/10.1021/acscentsci.8b00879> (accessed 26 May 2023).
39. B. Enderby et al., “Concentrations of some metabolites in the breath of healthy children aged 7–18 years measured using selected ion flow tube mass spectrometry (SIFT-MS),” *J. Breath Res.* **3**(3), 036001 (2009).
40. A. Thomas et al., “Novel noninvasive identification of biomarkers by analytical profiling of chronic wounds using volatile organic compounds,” *Wound Repair Regen. Off. Publ. Wound Heal. Soc. Eur. Tissue Repair Soc.* **18**, 391–400 (2010).
41. J. Williams and J. Pleil, “Crowd-based breath analysis: assessing behavior, activity, exposures, and emotional response of people in groups,” *J. Breath Res.* **10**(3), 032001 (2016).
42. R. Zuccarelli et al., “Multifaceted roles of nitric oxide in tomato fruit ripening: no-induced metabolic rewiring and consequences for fruit quality traits,” *J. Exp. Bot.* **72**(3), 941–958 (2021).
43. S. P. Singh, Z. Singh, and E. E. Swinny, “Postharvest nitric oxide fumigation delays fruit ripening and alleviates chilling injury during cold storage of Japanese plums (*Prunus salicina* Lindell),” *Postharvest Biol. Technol.* **53**(3), 101–108 (2009).
44. S. P. Burg and E. A. Burg, “Ethylene action and the ripening of fruits,” *Science* **148**(3674), 1190–1196 (1965).
45. M. M. Blanke, “Reducing ethylene levels along the food supply chain: a key to reducing food waste?” *J. Sci. Food Agric.* **94**(12), 2357–2361 (2014).
46. J. Sauer et al., “Continuous measurements of volatile gases as detection of algae crop health,” *Proc. Natl. Acad. Sci. U. S. A.* **118**, e2106882118 (2021).
47. WebMD, “Kidney failure (uremia) symptoms in cats,” <https://www.facebook.com/WebMD; https://pets.webmd.com/cats/kidney-failure-uremia-symptoms-cats> (accessed 26 May 2023).
48. E. E. Fabian, “Detecting ammonia in poultry housing using inexpensive instruments,” <https://extension.psu.edu/detecting-ammonia-in-poultry-housing-using-inexpensive-instruments> (accessed 26 May 2023).
49. K. G. Furton et al., “Advances in the use of odour as forensic evidence through optimizing and standardizing instruments and canines,” *Philos. Trans. R. Soc. B Biol. Sci.* **370**(1674), 20140262 (2015).
50. U.S. Wants Makers of Chinese Drywall to Fix U.S. Homes, “Reuters,” (January 10, 2011). <https://www.reuters.com/article/china-us-safety-idUKTOE70903220110110> (accessed 26 May 2023).
51. C. Love et al., “A review on advanced sensing materials for agricultural gas sensors,” *Sensors* **21**(10), 3423 (2021).
52. K. S. Santhanam and N. N. N. Ahamed, “Greenhouse gas sensors fabricated with new materials for climatic usage: a review,” *ChemEngineering* **2**(3), 38 (2018).

53. X. Chen et al., “Nanostructured gas sensors: from air quality and environmental monitoring to healthcare and medical applications,” *Nanomaterials* **11**(8), 1927 (2021).
54. R. A. Potyrailo et al., “Wireless sensors and sensor networks for homeland security applications,” *Trends Anal. Chem.* **40**, 133–145 (2012).
55. A. A. Tomchenko, G. P. Harmer, and B. T. Marquis, “Detection of chemical warfare agents using nanostructured metal oxide sensors,” *Sens. Actuators B Chem.* **108**(1–2), 41–55 (2005).
56. A. D. Wilson, “Electronic-nose applications in forensic science and for analysis of volatile biomarkers in the human breath,” *J. Forensic Sci. Criminol.* **1**(S103), 1–21 (2014).
57. K. Takahashi and I. Sugimoto, “Remarks on emotion recognition using breath gas sensing system,” *Smart Sens. Sens. Technol.* **20**, 49–62 (2008).
58. J. Hodgkinson and R. P. Tatam, “Optical gas sensing: a review,” *Meas. Sci. Technol.* **24**(1), 012004 (2012).
59. D. E. Williams, “Conduction and gas response of semiconductor gas sensors,” In *Solid State Gas Sensors*, P. T. Moseley and B. C. Toffield, Eds., 71–123, Hilger, Bristol (1987).
60. E. Bakker and M. Telting-Diaz, “Electrochemical sensors,” *Anal. Chem.* **74**(12), 2781–2800 (2002).
61. G. Korotcenkov, V. Brinzari, and M. H. Ham, “Materials acceptable for gas sensor design: advantages and limitations,” *Key Eng. Mater.* **780**, 80–89 (2018).
62. A. Caron et al., “Performances and limitations of electronic gas sensors to investigate an indoor air quality event,” *Build. Environ.* **107**, 19–28 (2016).
63. J. Wojtanowski et al., “Optical stand-off detection of biological and chemical hazards—prospects and concerns,” in *Baltic URSI Symp. (URSI)*, pp 100–105 (2018).
64. M. Kumar et al., “Stand-off detection of solid targets with diffuse reflection spectroscopy using a high-power mid-infrared supercontinuum source,” *Appl. Opt.* **51**(15), 2794–2807 (2012).
65. H. Huang et al., “In situ detection of gastrointestinal inflammatory biomarkers using electrochemical gas sensors,” in *44th Annu. Int. Conf. of the IEEE Eng. in Med. & Biol. Soc. (EMBC)*, pp. 2491–2494 (2022).
66. Y. Chen et al., “A flexible gastric gas sensor based on functionalized optical fiber,” *IEEE Sens. J.* **16**(13), 5243–5248 (2016).
67. Z. Liang et al., “Study on interference suppression algorithms for electronic noses: a review,” *Sensors* **18**(4), 1179 (2018).
68. J. Zhang et al., “A miniaturized electronic nose with artificial neural network for anti-interference detection of mixed indoor hazardous gases,” *Sens. Actuators B Chem.* **326**, 128822 (2021).
69. G. Man, B. Stoerber, and K. Walus, “An assessment of sensing technologies for the detection of clandestine methamphetamine drug laboratories,” *Forensic Sci. Int.* **189**(1), 1–13 (2009).
70. R. S. Kemp, “Environmental detection of clandestine nuclear weapon programs,” *Annu. Rev. Earth Planet. Sci.* **44**(1), 17–35 (2016).
71. N. Fabricius, G. Gauglitz, and J. Ingenhoff, “A gas sensor based on an integrated optical Mach-Zehnder interferometer,” *Sens. Actuators B Chem.* **7**(1), 672–676 (1992).
72. S. Khan, D. Newport, and S. Le Calvé, “Gas detection using portable deep-UV absorption spectrophotometry: a review,” *Sensors* **19**(23), 5210 (2019).
73. R. Ríos-Reina and S. M. Azcarate, “How chemometrics revives the UV-Vis spectroscopy applications as an analytical sensor for spectralprint (nontargeted) analysis,” *Chemosensors* **11**(1), 8 (2023).
74. R. Epping and M. Koch, “On-site detection of volatile organic compounds (VOCs),” *Molecules* **28**(4), 1598 (2023).
75. W. Göpel, “Entwicklung Chemischer Sensoren: Empirische Kunst Oder Systematische Forschung?/ Development of Chemical Sensors: Empirical Art or Systematic Research?” *tm - Technisches Messen* **52**(2), 47–58 (1985).
76. W. Gopel, “Chemisorption and charge transfer at ionic semiconductor surfaces: implications in designing gas sensors,” *Prog. Surf. Sci.* **20**(1), 9–103 (1985).
77. A. Gurlo and R. Riedel, “In situ and operando spectroscopy for assessing mechanisms of gas sensing,” *Angew. Chem. Int. Ed.* **46**(21), 3826–3848 (2007).
78. A. K. Goyal, H. S. Dutta, and S. Pal, “Recent advances and progress in photonic crystal-based gas sensors,” *J. Phys. Appl. Phys.* **50**(20), 203001 (2017).
79. Z. Wang et al., “Metal–organic framework-based photonic crystal platforms for gas sensing: a review,” *Mater. Adv.* **3**(17), 6728–6741 (2022).
80. T. W. Bell and N. M. Hext, “Supramolecular optical chemosensors for organic analytes,” *Chem. Soc. Rev.* **33**(9), 589–598 (2004).
81. M. Nguyen et al., “Dynamic plasmonic platform to investigate the correlation between far-field optical response and SERS signal of analytes,” *ACS Omega* **4**(1), 1144–1150 (2019).
82. J. White et al., “Rapid analyte recognition in a device based on optical sensors and the olfactory system,” *Anal. Chem.* **68**(13), 2191–2202 (1996).



83. R. A. Potyrailo and G. M. Hieftje, "Optical time-of-flight chemical detection: absorption-modulated fluorescence for spatially resolved analyte mapping in a bidirectional distributed fiber-optic sensor," *Anal. Chem.* **70**(16), 3407–3412 (1998).
84. J. Goh et al., "Diffraction-based assay for detecting multiple analytes," *Anal. Bioanal. Chem.* **374**(1), 54–56 (2002).
85. A. Dubrow et al., "Suppressing nonspecific binding in bilayer interferometry experiments for weak ligand–analyte interactions," *ACS Omega* **7**(11), 9206–9211 (2022).
86. D. A. Skoog, *Principles of Instrumental Analysis*, 4th ed., Saunders College Publishing, Fort Worth (1992).
87. Beer, "Bestimmung Der Absorption Des Rothen Lichts in Farbigen Flüssigkeiten," *Ann. Phys.* **162**(5), 78–88 (1852).
88. J. H. Lambert, *1728-1777. I.H. Lambert Photometria, Sive, De Mensura et Gradibus Luminis, Colorum et Umbrae [Microform]*, Landmarks of Science; V.E. Klett, Augustae Vindelicorum (1760).
89. D. K. Carpenter, "Physical Chemistry (Atkins, P. W.)," *J. Chem. Educ.* **56**(8), A260 (1979).
90. G. R. Choppin, "Studies of the hydrogen bonded structures of water and methanol," *J. Mol. Struct.* **45**, 39–54 (1978).
91. D. E. Lee et al., "Interferometer refractive index sensor based on a plasmonic channel waveguide," *Sensors* **17**(11), 2584 (2017).
92. R. P. W. Scott, "Chapter 2 the refractive index detector," in *Journal of Chromatography Library*, R. P. W. Scott, Ed., Vol. **11**, pp. 59–67, Elsevier (1977).
93. E. Hecht, *Optics*, 4th ed., Addison-Wesley, Reading, MA (2002).
94. X. Liu et al., "Measuring the refractive index of scintillation crystal with a Mach-Zehnder interferometer," *Opt. Contin.* **1**(4), 909–918 (2022).
95. Y. Xie, M. Zhang, and D. Dai, "Design rule of Mach-Zehnder interferometer sensors for ultra-high sensitivity," *Sensors* **20**(9), 2640 (2020).
96. S. O. Kasap et al., "Fundamental optical properties of materials II," in *Optical Properties of Materials and Their Applications*, J. Singh, Ed., pp. 37–65, John Wiley & Sons Ltd. (2019).
97. A. P. Wills, "The theory of electrons and its applications to the phenomena of light and radiant heat. By H. A. Lorentz," *Science* **31**(789), 221–223 (1910).
98. M. Fox, *Optical Properties of Solids*, World Scientific (2002).
99. J. Strong, "Principles of Optics. Electromagnetic Theory of Propagation, Interference and Diffraction of Light. Max Born, Emil Wolf et al. Pergamon Press, New York, 1959. Xxvi + 803 Pp. Illus. \$17.50," *Science* **131**, 495–495 (1960).
100. M. P. Givens, "Optical properties of metals," in *Solid State Physics*, F. Seitz and D. Turnbull, Eds., Vol. **6**, pp. 313–352, Academic Press (1958).
101. S. Moroni, D. M. Ceperley, and G. Senatore, "Static response and local field factor of the electron gas," *Phys. Rev. Lett.* **75**(4), 689–692 (1995).
102. P. Drude, "Zur Elektronentheorie Der Metalle," *Ann. Phys.* **306**(3), 566–613 (1900).
103. W. L. Bade, "Drude-model calculation of dispersion forces. I. General theory," *J. Chem. Phys.* **27**(6), 1280–1284 (1957).
104. H. Ibach and H. Lüth, "'Free' electrons in solids," in *Solid-State Physics: An Introduction to Principles of Materials Science*, H. Ibach and H. Lüth, Eds., pp. 135–158, Springer Berlin Heidelberg, Berlin, Heidelberg (2009).
105. L. Tonks and I. Langmuir, "Oscillations in ionized gases," *Phys. Rev.* **33**(2), 195–210 (1929).
106. B. Huffman, "Absorption and scattering by a sphere," in *Absorption and Scattering of Light by Small Particles*, pp. 82–129, WILEY-VCH Verlag GmbH & Co. KGaA (1998).
107. S. Zeng et al., "Nanomaterials enhanced surface plasmon resonance for biological and chemical sensing applications," *Chem. Soc. Rev.* **43**(10), 3426–3452 (2014).
108. "Near-field optical probes," in *Principles of Nano-Optics*, B. Hecht and L. Novotny, Eds., pp. 173–224, Cambridge University Press, Cambridge (2006).
109. J. D. Joannopoulos et al., *Photonic Crystals: Molding the Flow of Light*, Princeton University Press (2008).
110. J. D. Joannopoulos et al., *Photonic Crystals*, REV-Revised, 2nd ed., Princeton University Press (2008).
111. A. M. Fox, *Optical Properties of Solids*, Oxford University Press, Oxford (2002).
112. D. G. Lamas et al., "Nanostructured ceramic materials: applications in gas sensors and solid-oxide fuel cells," *J. Alloys Compd.* **495**(2), 548–551 (2010).
113. H. Kogelnik, "Theory of dielectric waveguides," in *Integrated Optics*, T. Tamir, Ed., pp. 13–81, Springer Berlin Heidelberg, Berlin, Heidelberg (1975).
114. E. Snitzer, "Cylindrical dielectric waveguide modes," *J. Opt. Soc. Am.* **51**(5), 491–498 (1961).
115. F. Frezza, A. Galli, and P. Lampariello, "Coupling and quality factors in parallelepiped nonradiative dielectric resonators," *Int. J. Infrared Millim. Waves* **17**(1), 137–152 (1996).
116. F. Wang, A. B. F. Martinson, and H. Harutyunyan, "Efficient nonlinear metasurface based on nonplanar plasmonic nanocavities," *ACS Photonics* **4**(5), 1188–1194 (2017).

117. J. Hong et al., “Nonlocal metasurface for circularly polarized light detection,” *Optica* **10**(1), 134–141 (2023).
118. M. Quinten, “Optical constants of gold and silver clusters in the spectral range between 1.5 eV and 4.5 eV,” *Z. Für Phys. B Condens. Matter* **101**(2), 211–217 (1996).
119. H.-J. Münzer et al., “Local field enhancement effects for nanostructuring of surfaces,” *J. Microsc.* **202**(1), 129–135 (2001).
120. H. K. Lee et al., “Designing surface-enhanced Raman scattering (SERS) platforms beyond hotspot engineering: emerging opportunities in analyte manipulations and hybrid materials,” *Chem. Soc. Rev.* **48**(3), 731–756 (2019).
121. R. Carles et al., “Three dimensional design of silver nanoparticle assemblies embedded in dielectrics for Raman spectroscopy enhancement and dark-field imaging,” *ACS Nano* **5**(11), 8774–8782 (2011).
122. E. J. Blackie, E. C. Le Ru, and P. G. Etchegoin, “Single-molecule surface-enhanced Raman spectroscopy of nonresonant molecules,” *J. Am. Chem. Soc.* **131**(40), 14466–14472 (2009).
123. E. C. Le Ru et al., “Surface enhanced Raman scattering enhancement factors: a comprehensive study,” *J. Phys. Chem. C* **111**(37), 13794–13803 (2007).
124. N. S. Lynn, Jr. and J. Homola, “(Bio)sensing using nanoparticle arrays: on the effect of analyte transport on sensitivity,” *Anal. Chem.* **88**(24), 12145–12151 (2016).
125. A. Tittl, H. Giessen, and N. Liu, “Plasmonic gas and chemical sensing,” *Nanophotonics* **3**(3), 157–180 (2014).
126. P. Hlubina et al., “Ultrahigh-sensitive plasmonic sensing of gas using a two-dimensional dielectric grating,” *Opt. Lett.* **44**(22), 5602–5605 (2019).
127. E. Kretschmann, “The angular dependence and the polarisation of light emitted by surface plasmons on metals due to roughness,” *Opt. Commun.* **5**(5), 331–336 (1972).
128. A. Biswas et al., “Advances in top–down and bottom–up surface nanofabrication: techniques, applications & future prospects,” *Adv. Colloid Interface Sci.* **170**(1), 2–27 (2012).
129. R. Jannesari et al., “Hybrid photonic crystal-surface plasmon polariton waveguiding system for on-chip sensing applications,” *Proceedings* **2**(13), 864 (2018).
130. A. Sharma, R. Jha, and B. Gupta, “Fiber-optic sensors based on surface plasmon resonance: a comprehensive review,” *Sens. J. IEEE* **7**, 1118–1129 (2007).
131. A. L. Ingram and A. R. Parker, “A review of the diversity and evolution of photonic structures in butterflies, incorporating the work of John Huxley (The Natural History Museum, London from 1961 to 1990),” *Philos. Trans. R. Soc. B Biol. Sci.* **363**(1502), 2465–2480 (2008).
132. S. C. Burgess, A. King, and R. Hyde, “An analysis of optimal structural features in the peacock tail feather,” *Opt. Laser Technol.* **38**(4–6), 329–334 (2006).
133. J. Zi et al., “Coloration strategies in peacock feathers,” *Proc. Natl. Acad. Sci. U. S. A.* **100**(22), 12576–12578 (2003).
134. S. Yoshioka and S. Kinoshita, “Effect of macroscopic structure in iridescent color of the peacock feathers,” *Forma* **17**(2), 169–181 (2002).
135. Y. Wang et al., “Study on the microstructure and its coloration mechanism of peacock feather by the FDTD method,” *J. Phys. Conf. Ser.* **1549**(3), 032036 (2020).
136. T. Ueta et al., “Numerical study on the structural color of blue birds by a disordered porous photonic crystal model,” *Eur. Lett.* **107**(3), 34004 (2014).
137. C. D’Ambrosio et al., “Structural color in the swallow tanager (*Tersina viridis*): using the Korringa-Kohn-Rostoker method to simulate disorder in natural photonic crystals,” *Phys. Rev. E* **98**(3), 7 (2018).
138. M. Kolle and S. Lee, “Progress and opportunities in soft photonics and biologically inspired optics,” *Adv. Mater.* **30**(2), 1702669 (2018).
139. M. Diab and T. Mokari, “Bioinspired hierarchical porous structures for engineering advanced functional inorganic materials,” *Adv. Mater.* **30**(41), 1706349 (2018).
140. D. Vine et al., “Domain morphology, boundaries, and topological defects in biophotonic gyroid nanostructures of butterfly wing scales,” *Sci. Adv.* **2**(6), e1600149 (2016).
141. R. T. Lee and G. S. Smith, “Detailed electromagnetic simulation for the structural color of butterfly wings,” *Appl. Opt.* **48**(21), 4177–4190 (2009).
142. M. A. Steindorfer et al., “Detailed simulation of structural color generation inspired by the *Morpho* butterfly,” *Opt. Express* **20**(19), 21485 (2012).
143. B. Gralak, G. Tayeb, and S. Enoch, “*Morpho* butterflies wings color modeled with lamellar grating theory,” *Opt. Express* **9**(11), 567 (2001).
144. X. Yang et al., “Using hierarchy architecture of *Morpho* butterfly scales for chemical sensing: experiment and modeling,” *Sens. Actuators Phys.* **167**(2), 367–373 (2011).
145. Q. Li et al., “Bio-inspired sensors based on photonic structures of *Morpho* butterfly wings: a review,” *J. Mater. Chem. C* **4**(9), 1752–1763 (2016).
146. B. Song et al., “Reproducing the hierarchy of disorder for *Morpho*-inspired, broad-angle color reflection,” *Sci. Rep.* **7**(1), 46023 (2017).

147. S. Kinoshita, S. Yoshioka, and K. Kawagoe, "Mechanisms of structural colour in the *Morpho* butterfly: cooperation of regularity and irregularity in an iridescent scale," *Proc. R. Soc. Lond. B Biol. Sci.* **269**(1499), 1417–1421 (2002).
148. C. M. Soukoulis, "The history and a review of the modelling and fabrication of photonic crystals," *Nanotechnology* **13**(3), 420 (2002).
149. U. Biswas, C. Nayak, and J. K. Rakshit, "Fabrication techniques and applications of two-dimensional photonic crystal: history and the present status," *Opt. Eng.* **62**(1), 010901 (2023).
150. C. M. Soukoulis, *Photonic Crystals and Light Localization in the 21st Century*, Vol. **563**, Springer Science & Business Media (2012).
151. Z. Cai et al., "From colloidal particles to photonic crystals: advances in self-assembly and their emerging applications," *Chem. Soc. Rev.* **50**(10), 5898–5951 (2021).
152. S. Takahashi et al., "Direct creation of three-dimensional photonic crystals by a top-down approach," *Nat. Mater.* **8**(9), 721–725 (2009).
153. G. von Freymann et al., "Bottom-up assembly of photonic crystals," *Chem. Soc. Rev.* **42**(7), 2528–2554 (2013).
154. P. Ferrand et al., "Direct electron-beam lithography on opal films for deterministic defect fabrication in three-dimensional photonic crystals," *Microelectron. Eng.* **73–74**, 362–366 (2004).
155. M. Belotti et al., "Investigation of SOI photonic crystals fabricated by both electron-beam lithography and nanoimprint lithography," *Microelectron. Eng.* **73–74**, 405–411 (2004).
156. G. Subramania and S. Y. Lin, "Fabrication of three-dimensional photonic crystal with alignment based on electron beam lithography," *Appl. Phys. Lett.* **85**(21), 5037–5039 (2004).
157. M. Campbell et al., "Fabrication of photonic crystals for the visible spectrum by holographic lithography," *Nature* **404**(6773), 53–56 (2000).
158. J. Li et al., "Fabrication of photonic crystals with functional defects by one-step holographic lithography," *Opt. Express* **16**(17), 12899–12904 (2008).
159. L. Wu, Y. Xu, and K. S. Wong, "Fabrication of photonic crystals using holographic lithography," in *Organic and Hybrid Photonic Crystals*, D. Comoretto, Ed., pp. 213–239, Springer International Publishing, Cham (2015).
160. J. H. Moon, J. Ford, and S. Yang, "Fabricating three-dimensional polymeric photonic structures by multi-beam interference lithography," *Polym. Adv. Technol.* **17**(2), 83–93 (2006).
161. P. Lova and C. Soci, "Nanoimprint lithography: toward functional photonic crystals," in *Organic and Hybrid Photonic Crystals*, D. Comoretto, Ed., pp. 187–212, Springer (2015).
162. S. Barcelo and Z. Li, "Nanoimprint lithography for nanodevice fabrication," *Nano Converg.* **3**(1), 1–9 (2016).
163. J. F. Galisteo-López et al., "Self-assembled photonic structures," *Adv. Mater.* **23**(1), 30–69 (2011).
164. J. H. Holtz and S. A. Asher, "Polymerized colloidal crystal hydrogel films as intelligent chemical sensing materials," *Nature* **389**(6653), 829–832 (1997).
165. A. Anopchenko et al., "Effect of thickness disorder on the performance of photonic crystal surface wave sensors," *Opt. Express* **24**(7), 7728–7742 (2016).
166. A. Potyrai et al., "Bio-inspired gas sensing: boosting performance with sensor optimization guided by "machine learning"," *Faraday Discuss.* **223**, 161–182 (2020).
167. L. O'Faolain et al., "Low-loss propagation in photonic crystal waveguides," *Electron. Lett.* **42**(25), 1454–1455 (2006).
168. H. Duan et al., "Sub-10-Nm half-pitch electron-beam lithography by using poly(methyl methacrylate) as a negative resist," *J. Vac. Sci. Technol. B Nanotechnol. Microelectron. Mater. Process. Meas. Phenom.* **28**(6), C6C58–C6C62 (2010).
169. V. R. Manfrinato et al., "Resolution limits of electron-beam lithography toward the atomic scale," *Nano Lett.* **13**(4), 1555–1558 (2013).
170. R. F. W. Pease, "Electron beam lithography," *Contemp. Phys.* **22**(3), 265–290 (1981).
171. L. Wang et al., "Fabrication of three-dimensional (3D) woodpile structure photonic crystal with layer by layer e-beam lithography," *Appl. Phys. A* **95**(2), 329–334 (2009).
172. V. Ray et al., "High resolution patterning on nonplanar substrates with large height variation using electron beam lithography," *J. Vac. Sci. Technol. B* **30**(6), 06F303 (2012).
173. W. L. Brown, T. Venkatesan, and A. Wagner, "Ion beam lithography," *Nucl. Instrum. Methods Phys. Res.* **191**(1), 157–168 (1981).
174. J. Melngailis, "Focused ion beam lithography," *Nucl. Instrum. Methods Phys. Res. Sect. B Beam Interact. Mater. At.* **80–81**, 1271–1280 (1993).
175. J. Igaki et al., "Comparison of FIB-CVD and EB-CVD growth characteristics," *Microelectron. Eng.* **83**(4–9), 1225–1228 (2006).
176. J. Fujita et al., "Growth of three-dimensional nano-structures using FIB-CVD and its mechanical properties," *Nucl. Instrum. Methods Phys. Res. Sect. B Beam Interact. Mater. At.* **206**, 472–477 (2003).

177. M. Wang, Ed., *Lithography*, IntechOpen, Rijeka (2010).
178. E. Sharma et al., "Evolution in lithography techniques: microlithography to nanolithography," *Nanomaterials* **12**(16), 2754 (2022).
179. Y. Nishimura et al., "Photolithography," in *Flat Panel Display Manufacturing*, J. Souk et al., Eds., pp. 287–310, John Wiley & Sons Ltd. (2018).
180. M. C. King and D. H. Berry, "Photolithographic mask alignment using Moiré techniques," *Appl. Opt.* **11**(11), 2455–2459 (1972).
181. J. Rasson et al., "Vapor sensing using a bio-inspired porous silicon photonic crystal," *Mater. Today Proc.* **4**(4), 5006–5012 (2017).
182. R. A. Potyrailo et al., "Multivariable bio-inspired photonic sensors for non-condensable gases," *J. Opt.* **20**(2), 024006 (2018).
183. C. Lu and R. H. Lipson, "Interference lithography: a powerful tool for fabricating periodic structures," *Laser Photonics Rev.* **4**(4), 568–580 (2010).
184. L. Z. Cai, X. L. Yang, and Y. R. Wang, "All fourteen Bravais lattices can be formed by interference of four noncoplanar beams," *Opt. Lett.* **27**(11), 900–902 (2002).
185. R. H. Siddique et al., "Fabrication of hierarchical photonic nanostructures inspired by *Morpho* butterflies utilizing laser interference lithography," *Opt. Mater. Express* **5**(5), 996–1005 (2015).
186. P. A. Snow et al., "Vapor sensing using the optical properties of porous silicon Bragg mirrors," *J. Appl. Phys.* **86**(4), 1781–1784 (1999).
187. V. S. Lin et al., "A porous silicon-based optical interferometric biosensor," *Science* **278**(5339), 840–843 (1997).
188. G.-G. Liu et al., "Topological Anderson insulator in disordered photonic crystals," *Phys. Rev. Lett.* **125**(13), 133603 (2020).
189. Y. A. Vlasov, M. Kaliteevski, and V. Nikolaev, "Different regimes of light localization in a disordered photonic crystal," *Phys. Rev. B* **60**(3), 1555 (1999).
190. F. Zhang et al., "Infrared detection based on localized modification of *Morpho* butterfly wings," *Adv. Mater.* **27**(6), 1077–1082 (2015).
191. G. Piszter et al., "Substance specific chemical sensing with pristine and modified photonic nanoarchitectures occurring in blue butterfly wing scales," *Opt. Express* **22**(19), 22649–22660 (2014).
192. A. Abbaszadeh, S. Makouei, and S. Meshgini, "High sensitive triangular photonic crystal fiber sensor design applicable for gas detection," *Adv. Electromagn.* **10**(1) (2021).
193. M. Appold and M. Gallei, "Bio-inspired structural colors based on linear ultrahigh molecular weight block copolymers," *ACS Appl. Polym. Mater.* **1**(2), 239–250 (2019).
194. L. Bai et al., "Bio-inspired vapor-responsive colloidal photonic crystal patterns by inkjet printing," *ACS Nano* **8**(11), 11094–11100 (2014).
195. S. Asaduzzaman, B. K. Paul, and K. Ahmed, "Enhancement of sensitivity and birefringence of a gas sensor on micro-core based photonic crystal fiber," in *3rd Int. Conf. Electr. Eng. Inf. Commun. Technol. ICEEICT Electr. Eng. Inf. Commun. Technol. ICEEICT 2016 3rd Int. Conf. On*, pp. 1–4 (2016).
196. B. K. Paul et al., "Investigation of gas sensor based on differential optical absorption spectroscopy using photonic crystal fiber," *Alex. Eng. J.* **59**(6), 5045–5052 (2020).
197. A. M. Cubillas et al., "Methane detection at 1670-Nm band using a hollow-core photonic bandgap fiber and a multiline algorithm," *Opt. Express* **15**(26), 17570–17576 (2007).
198. X. Qin et al., "Molybdenum sulfide/citric acid composite membrane-coated long period fiber grating sensor for measuring trace hydrogen sulfide gas," *Sens. Actuators B Chem.* **272**, 60–68 (2018).
199. B. Xu et al., "Ultrasensitive NO gas sensor based on the graphene oxide-coated long-period fiber grating," *ACS Appl. Mater. Interfaces* **11**(43), 40868–40874 (2019).
200. W. Wei et al., "Graphene-based long-period fiber grating surface plasmon resonance sensor for high-sensitivity gas sensing," *Sensors* **17**(12), 2 (2016).
201. H. Hu et al., "Characterization of infrared gas sensors employing hollow-core photonic crystal fibers," *Instrum. Sci. Technol.* **44**(5), 495–503 (2016).
202. B. M. Masum et al., "Gas sensing with hollow-core photonic crystal fibres: a comparative study of mode analysis and gas flow performance," *Photonics Nanostruct. - Fundam. Appl.* **41**, 100830 (2020).
203. M. R. Sardar, M. Faisal, and K. Ahmed, "Simple hollow core photonic crystal fiber for monitoring carbon dioxide gas with very high accuracy," *Sens. Bio-Sens. Res.* **31**, 100401 (2021).
204. Md. R. Sardar and M. Faisal, "Gas sensor based on octagonal hollow core photonic crystal fiber," in *IEEE Int. Conf. Imaging Vis. Pattern Recognit. ICIIVPR Imaging Vis. Pattern Recognit. ICIIVPR 2017 IEEE Int. Conf. On*, pp. 1–4 (2017).
205. P. Steinvurzel et al., "Long period grating resonances in photonic bandgap fiber," *Opt. Express* **14**(7), 3007–3014 (2006).
206. Y. Zhu, "Long-period gratings in photonic crystal fiber: fabrication, characterization, and potential applications for gas sensing," *Proc. SPIE* **6005**, 60050K (2005).

207. L. Qi et al., "Highly reflective long period fiber grating sensor and its application in refractive index sensing," *Sens. Actuators B Chem.* **193**, 185–189 (2014).
208. F. Esposito et al., "Label-free biosensors based on long period fiber gratings: a review," *IEEE Sens. J.* **21**(11), 12692–12705 (2020).
209. M. Janczuk-Richter et al., "Long-period fiber grating sensor for detection of viruses," *Sens. Actuators B Chem.* **250**, 32–38 (2017).
210. L. Rindorf et al., "Photonic crystal fiber long-period gratings for biochemical sensing," *Opt. Express* **14**(18), 8224–8231 (2006).
211. S. R. Mouchet et al., "Controlled fluorescence in a beetle's photonic structure and its sensitivity to environmentally induced changes," *Proc. R. Soc. B Biol. Sci.* **283**(1845), 20162334 (2016).
212. M. Qi et al., "A three-dimensional optical photonic crystal with designed point defects," *Nature* **429**(6991), 538–542 (2004).
213. C. Kang and S. M. Weiss, "Photonic crystal with multiple-hole defect for sensor applications," *Opt. Express* **16**(22), 18188–18193 (2008).
214. T. L. Kelly, A. Garcia Segua, and M. J. Sailor, "Identification and quantification of organic vapors by time-resolved diffusion in stacked mesoporous photonic crystals," *Nano Lett.* **11**(8), 3169–3173 (2011).
215. F. Belén et al., "NIR-reflective and hydrophobic bio-inspired nano-holed configurations on titanium alloy," *ACS Appl. Mater. Interfaces* **14**(4), 5843–5855 (2022).
216. E. Menumerov et al., "Sensing hydrogen gas from atmospheric pressure to a hundred parts per million with nanogaps fabricated using a single-step bending deformation," *ACS Sens.* **1**(1), 73–80 (2016).
217. R. A. Potyrailo et al., "Discovery of the surface polarity gradient on iridescent *Morpho* butterfly scales reveals a mechanism of their selective vapor response," *Proc. Natl. Acad. Sci.* **110**(39), 15567–15572 (2013).
218. R. A. Potyrailo et al., "*Morpho* butterfly wing scales demonstrate highly selective vapour response," *Nat. Photonics* **1**(2), 123–128 (2007).
219. S. Kinoshita et al., "Photophysics of structural color in the *Morpho* butterflies," undefined (2002).
220. E. Kuramochi et al., "Disorder-induced scattering loss of line-defect waveguides in photonic crystal slabs," *Phys. Rev. B* **72**(16), 161318 (2005).
221. M. Patterson et al., "Disorder-induced incoherent scattering losses in photonic crystal waveguides: Bloch mode reshaping, multiple scattering, and breakdown of the Beer-Lambert law," *Phys. Rev. B* **80**(19), 195305 (2009).
222. M. Lončar, A. Scherer, and Y. Qiu, "Photonic crystal laser sources for chemical detection," *Appl. Phys. Lett.* **82**(26), 4648–4650 (2003).
223. G. Guida, "Numerical studies of disordered photonic crystals," *Prog. Electromagn. Res.* **41**, 107–131 (2003).
224. V. Savona, "Electromagnetic modes of a disordered photonic crystal," *Phys. Rev. B* **83**(8), 085301 (2011).
225. M. Skorobogatiy, G. Bégin, and A. Talneau, "Statistical analysis of geometrical imperfections from the images of 2D photonic crystals," *Opt. Express* **13**(7), 2487–2502 (2005).
226. G. I. Mark et al., "Order-disorder effects in structure and color relation of photonic-crystal-type nanostructures in butterfly wing scales," *Phys. Rev. E* **80**(5 Pt 1), 051903 (2009).
227. S. Amrehn, X. Wu, and T. Wagner, "Tungsten oxide photonic crystals as optical transducer for gas sensing," *ACS Sens.* **3**(1), 191–199 (2018).
228. J. Knight et al., "Properties of photonic crystal fiber and the effective index model," *JOSA A* **15**(3), 748–752 (1998).
229. T. A. Birks, J. C. Knight, and P. S. J. Russell, "Endlessly single-mode photonic crystal fiber," *Opt. Lett.* **22**(13), 961–963 (1997).
230. C. Markos et al., "Hybrid photonic-crystal fiber," *Rev. Mod. Phys.* **89**(4), 045003 (2017).
231. J. Hou et al., "Flat band slow light in symmetric line defect photonic crystal waveguides," *IEEE Photonic Technol. Lett.* **21**(20), 1571–1573 (2009).
232. A. Lavrinenko et al., "Comprehensive FDTD modelling of photonic crystal waveguide components," *Opt. Express* **12**(2), 234–248 (2004).
233. N. Skivesen et al., "Photonic-crystal waveguide biosensor," *Opt. Express* **15**(6), 3169–3176 (2007).
234. L. H. Frandsen et al., "Photonic crystal waveguides with semi-slow light and tailored dispersion properties," *Opt. Express* **14**(20), 9444–9450 (2006).
235. O. Painter et al., "Two-dimensional photonic band-gap defect mode laser," *Science* **284**(5421), 1819 (1999).
236. T. Ali et al., "A thin-film flexible defect-mode laser," *Adv. Opt. Mater.* **8**(8), 1901891 (2020).
237. Y. Matsuhisa et al., "High Q defect mode and laser action in one-dimensional hybrid photonic crystal containing cholesteric liquid crystal," *Appl. Phys. Lett.* **89**(10), 101109 (2006).
238. M. Imada et al., "Channel drop filter using a single defect in a 2-D photonic crystal slab waveguide," *J. Lightwave Technol.* **20**(5), 873–878 (2002).
239. O. Painter, J. Vučković, and A. Scherer, "Defect modes of a two-dimensional photonic crystal in an optically thin dielectric slab," *JOSA B* **16**(2), 275–285 (1999).

240. D. Gerace and L. C. Andreani, "Disorder-induced losses in photonic crystal waveguides with line defects," *Opt. Lett.* **29**(16), 1897–1899 (2004).
241. P. Griffin, P. Nagel, and R. Koshel, "The plane-wave expansion method," *J. Math. Phys.* **15**(11), 1913–1917 (1974).
242. S. Shi, C. Chen, and D. W. Prather, "Plane-wave expansion method for calculating band structure of photonic crystal slabs with perfectly matched layers," *JOSA A* **21**(9), 1769–1775 (2004).
243. L. Kassa-Baghdouche and E. Cassan, "Mid-infrared gas sensor based on high-Q/V point-defect photonic crystal nanocavities," *Opt. Quantum Electron.* **52**(5), 1–13 (2020).
244. F. Scotognella, "One-dimensional photonic structure with multilayer random defect," *Opt. Mater.* **36**(2), 380–383 (2013).
245. M. Ishfak Tahmid, D. Joti Paul, and M. Zunaid Baten, "Emergence and tunability of transmission gap in the strongly disordered regime of a dielectric random scattering medium," *Opt. Express* **29**(11), 17215–17226 (2021).
246. S. Takeda, P. Viktorovtich, and M. Obara, *Anderson Localization of Light in Two-Dimensional Random Photonic Crystals*, Vol. **1**, IEEE (2011).
247. J. I. Chen et al., "Effect of disorder on the optically amplified photocatalytic efficiency of titania inverse opals," *J. Am. Chem. Soc.* **129**(5), 1196–1202 (2007).
248. S. R. Mouchet et al., "Optical costs and benefits of disorder in biological photonic crystals," *Faraday Discuss.* **223**, 9–48 (2020).
249. J. Topolancik, F. Vollmer, and B. Ilic, "Random high-Q cavities in disordered photonic crystal waveguides," *Appl. Phys. Lett.* **91**(20), 201102 (2007).
250. N. Mann et al., "Theory and experiments of disorder-induced resonance shifts and mode-edge broadening in deliberately disordered photonic crystal waveguides," *Phys. Rev. A* **92**(2), 023849 (2015).
251. L. S. Froufe-Pérez et al., "Band gap formation and Anderson localization in disordered photonic materials with structural correlations," *Proc. Natl. Acad. Sci.* **114**(36), 9570 (2017).
252. M. Sarabandi et al., "Localization mode selector based on disordered dielectric photonic crystal," *Opt. Commun.* **475**, 126263 (2020).
253. J. Topolancik, B. Ilic, and F. Vollmer, "Experimental observation of strong photon localization in disordered photonic crystal waveguides," *Phys. Rev. Lett.* **99**(25), 253901 (2012).
254. J. M. Rico-García, J. López-Alonso, and J. Alda, "Characterization of photonic crystal microcavities with manufacture imperfections," *Opt. Express* **13**(10), 3802–3815 (2005).
255. L. O'Faolain et al., "Dependence of extrinsic loss on group velocity in photonic crystal waveguides," *Opt. Express* **15**(20), 13129–13138 (2007).
256. K. Vynck et al., "Photon management in two-dimensional disordered media," *Nat. Mater.* **11**(12), 1017–1022 (2012).
257. X. Sheng et al., "Optimization-based design of surface textures for thin-film Si solar cells," *Opt. Express* **19**(S4), A841–A850 (2011).
258. V. E. Ferry et al., "Optimized spatial correlations for broadband light trapping nanopatterns in high efficiency ultrathin film A-Si:H solar cells," *Nano Lett.* **11**(10), 4239–4245 (2011).
259. C. Rockstuhl, U. Peschel, and F. Lederer, "Correlation between single-cylinder properties and bandgap formation in photonic structures," *Opt. Lett.* **31**(11), 1741–1743 (2006).
260. Y. Gao et al., "Sensitivity analysis of a bioinspired refractive index based gas sensor," *J. Bionic Eng.* **8**(3), 323–334 (2011).
261. J. D. Kittle et al., "Sensing chemical warfare agent simulants via photonic crystals of the *Morpho didius* butterfly," *ACS Omega* **2**(11), 8301–8307 (2017).
262. T. Starkey, "Towards bio-inspired photonic vapour sensors," School of Physics, University of Exeter (2014).
263. T. Jiang et al., "Gas sensing using hierarchical micro/nanostructures of *Morpho* butterfly scales," *Sens. Actuators Phys.* **213**, 63–69 (2014).
264. J. D. Kittle et al., "Sensing chemical warfare agent simulants via photonic crystals of the *Morpho didius* butterfly," *ACS Omega* **2**(11), 8301–8307 (2017).
265. H. Kim et al., "Structural colour printing using a magnetically tunable and lithographically fixable photonic crystal," *Nat. Photonics* **3**(9), 534–540 (2009).
266. A. R. Parker and H. E. Townley, "Biomimetics of photonic nanostructures," *Nat. Nanotechnol.* **2**(6), 347–353 (2007).
267. M. Rassart et al., "Diffractive hydrochromic effect in the cuticle of the Hercules beetle *Dynastes hercules*," *New J. Phys.* **10**(3), 033014 (2008).
268. P. A. Hiltner and I. M. Krieger, "Diffraction of light by ordered suspensions," *J. Phys. Chem.* **73**(7), 2386–2389 (1969).
269. S. G. Romanov et al., "Thin opaline photonic crystals," in *Photonic Crystals and Light Localization in the 21st Century*, C. M. Soukoulis, Ed., pp. 253–262, Springer Netherlands, Dordrecht (2001).
270. S. Kinoshita et al., "Photophysics of structural color in the *Morpho* butterflies," *Forma* **17**, 103–121 (2002).

271. J. Gao et al., "Vapor sensors based on optical interferometry from oxidized microporous silicon films," *Langmuir* **18**(6), 2229–2233 (2002).
272. M. R. Baklanov et al., "Determination of pore size distribution in thin films by ellipsometric porosimetry," *J. Vac. Sci. Technol. B Microelectron. Nanometer Struct. Process. Meas. Phenom.* **18**(3), 1385–1391 (2000).
273. H. Yang, P. Jiang, and B. Jiang, "Vapor detection enabled by self-assembled colloidal photonic crystals," *J. Colloid Interface Sci.* **370**(1), 11–18 (2012).
274. M. G. Moharam and T. K. Gaylord, "Rigorous coupled-wave analysis of planar-grating diffraction," *JOSA* **71**(7), 811–818 (1981).
275. H. Martens and M. Martens, *Multivariate Analysis of Quality: An Introduction*, Wiley, Chichester; New York (2001).
276. P. Vukusic et al., "Quantified interference and diffraction in single *Morpho* butterfly scales," *Proc. R. Soc. Lond. B Biol. Sci.* **266**(1427), 1403–1411 (1999).
277. X. Fan, W. Zheng, and D. J. Singh, "Light scattering and surface plasmons on small spherical particles," *Light Sci. Appl.* **3**(6), e179–e179 (2014).
278. L. Wang, M. Hasanzadeh Kafshgari, and M. Meunier, "Optical properties and applications of plasmonic-metal nanoparticles," *Adv. Funct. Mater.* **30**(51), 2005400 (2020).
279. T. Chen et al., "Tailoring plasmon coupling in self-assembled one-dimensional Au nanoparticle chains through simultaneous control of size and gap separation," *J. Phys. Chem. Lett.* **4**(13), 2147–2152 (2013).
280. S. Zeng et al., "Size dependence of Au NP-enhanced surface plasmon resonance based on differential phase measurement," *Sens. Actuators B Chem.* **176**, 1128–1133 (2013).
281. H. Butt et al., "*Morpho* butterfly-inspired nanostructures," *Adv. Opt. Mater.* **4**(4), 497–504 (2016).
282. A. D. Pris et al., "Towards high-speed imaging of infrared photons with bio-inspired nanoarchitectures," *Nat. Photonics* **6**(3), 195–200 (2012).
283. T. Lu et al., "Bioinspired thermoresponsive photonic polymers with hierarchical structures and their unique properties," *Macromol. Rapid Commun.* **36**(19), 1722–1728 (2015).
284. D. Xu et al., "Thermoresponsive photonic crystal: synergistic effect of poly(N-isopropylacrylamide)-co-acrylic acid and *Morpho* butterfly wing," *ACS Appl. Mater. Interfaces* **7**(16), 8750–8756 (2015).
285. X. Xu et al., "A near-infrared and temperature-responsive pesticide release platform through core-shell polydopamine@PNIPAm nanocomposites," *ACS Appl. Mater. Interfaces* **9**(7), 6424–6432 (2017).
286. Q. Shen et al., "Subtractive structural modification of *Morpho* butterfly wings," *Small* **11**(42), 5705–5711 (2015).
287. Y. Zhu, W. Zhang, and D. Zhang, "Fabrication of sensor materials inspired by butterfly wings," *Adv. Mater. Technol.* **2**(7), 1600209 (2017).
288. R. A. Potyrailo, P. Ottikkutti, and M. Nayeri, "Physical and analytical principles of multivariable gas and liquid sensors," in *IEEE SENSORS*, pp. 1–4 (2018).
289. R. A. Potyrailo et al., "Bio-inspired gas sensing: boosting performance with sensor optimization guided by "machine learning"," *Faraday Discuss.* **223**, 161–182 (2020).
290. T. Y. Jeon et al., "Nanostructured plasmonic substrates for use as SERS sensors," *Nano Converg.* **3**(1), 18 (2016).
291. J. Ding et al., "New sensor for gases dissolved in transformer oil based on solid oxide fuel cell," *Sens. Actuators B Chem.* **202**, 232–239 (2014).
292. Y. Ke et al., "Cephalopod-inspired versatile design based on plasmonic VO<sub>2</sub> nanoparticle for energy-efficient mechano-thermochromic windows," *Nano Energy* **73**, 104785 (2020).
293. L. Hajshahvaladi, H. Kaatuzian, and M. Danaie, "Design of a hybrid photonic-plasmonic crystal refractive index sensor for highly sensitive and high-resolution sensing applications," *Phys. Lett. A* **420**, 127754 (2021).
294. S. A. Maier, *Plasmonics: Fundamentals and Applications*, Vol. **76**, Springer (2004).
295. C. Qi et al., "Refractive index sensor based on photonic crystal nanocavity," *Opt. Commun.* **464**, 125393 (2020).
296. F. Baranzadeh and N. Nozhat, "High performance plasmonic nano-biosensor based on tunable ultra-narrowband perfect absorber utilizing liquid crystal," *Plasmonics* **16**(1), 253–262 (2021).
297. M. J. Rycroft, "Computational electrodynamics, the finite-difference time-domain method," *J. Atmos. Terr. Phys.* **58**(15), 1817–1818 (1996).
298. M. Danaie and A. Shahzadi, "Design of a high-resolution metal-insulator-metal plasmonic refractive index sensor based on a ring-shaped Si resonator," *Plasmonics* **14**(6), 1453–1465 (2019).
299. J.-Y. Ye et al., "Fabrication and optical characteristics of silicon-based two-dimensional photonic crystals with honeycomb lattice," *Opt. Commun.* **211**(1), 205–213 (2002).
300. P. B. Johnson and R. W. Christy, "Optical constants of the noble metals," *Phys. Rev. B* **6**, 4370 (1972).
301. Z. Mu et al., "FDTD modeling of photonic crystal-incorporated gold nanoparticles for enhancing the localized electric field," *J. Mater. Chem. C* **5**(37), 9540–9544 (2017).

302. Z. Mu et al., “Photonic crystal hydrogel enhanced plasmonic staining for multiplexed protein analysis,” *Small* **11**(45), 6036–6043 (2015).
303. Z. Mu et al., “In situ synthesis of gold nanoparticles (AuNPs) in butterfly wings for surface enhanced Raman spectroscopy (SERS),” *J. Mater. Chem. B* **1**(11), 1607–1613 (2013).
304. S.-Y. Ding et al., “Nanostructure-based plasmon-enhanced Raman spectroscopy for surface analysis of materials,” *Nat. Rev. Mater.* **1**(6), 1–16 (2016).

**Amanda L. Musgrove** worked alongside Dr. Jimmy E. Touma at the Air Force Research Laboratory (Eglin AFB, FL) with a research focus on bioinspired nanophotonics for sensor applications. Amanda is currently a staff research scientist at Oak Ridge National Laboratory in the Energy Storage group and studies interfacial reactions as well as the development of new materials and processes for energy storage and conversion applications.

**Alexander Cockerham** is a doctoral candidate at CREOL, the College of Optics and Photonics at the University of Central Florida. He is a member of the Nanophotonic Materials Group under Dr. Stephen Kuebler, and the Ultrafast Laser Processing Group under Dr. Xiaoming Yu. His research interests include the design and simulation of nanoscale optical devices such as meta-lenses and photonic crystals, and high-throughput fabrication of nanostructured materials using spatially shaped laser beams.

**Javier J. Pazos** is the President of Heroica Technologies, LLC, working on research and development of photonics and optical devices that leverage the latest developments in computational electromagnetics (CEM) and additive manufacturing. He previously served as the CEM lead at SpaceX, working on the design and analysis of launch assets for lightning and space charging certification. He has also served as a CEM engineer for Intel Corporation and Electro Magnetic Applications, Inc., a developer of time-domain software.

**Stephen M. Kuebler** is a professor of chemistry and optics at the University of Central Florida (UCF) and a founding associate director of the UCF Center for Ethics. He holds joint appointments in the Department of Chemistry; CREOL, The College of Optics and Photonics; and the Department of Materials Science. His group develops new materials and processes for 3D fabrication through multi-photon lithography and uses the technique to fabricate and investigate novel 3D nanophotonic devices.

**Jimmy E. Touma** is a senior physicist in the Electronics and Photonics Group at the Air Force Research Laboratory on Eglin AFB, FL. His group conducts and funds research in nanophotonics and both artificial and bioinspired metamaterials for sensor and seeker enhancements. His portfolio includes basic and applied research ranging from metalenses in the visible and IR bands to metamaterial multi-band RF antennas.

Biographies of the other authors are not available.